

Anonymous Referee #2 Received and published: 24 January 2018 Review of: Modern Banded Iron Sedimentary Rocks on Milos Island, Greece.

#### Comments

The manuscript is well written, though it does suffer from a smattering of grammatical mistakes.

**Responses:** We extend thankfulness to this reviewer for taking time off to read and comment on our manuscript. His comments have condensed the sedimentology, tightening up loose parts suffering from lack of clarity. To satisfy the comment about a smattering of grammatical errors, we have taken care to minimize errors that might previously have escaped careful editing. Attached to this document is a PDF file named, supplement, containing the manuscript with changes, including those requested by the reviews, in red.

The layers under study do seem somewhat similar to Precambrian BIFs and are thus worth investigation, though it must always be emphasized that Precambrian ocean chemistry was very different than today's seas. I have not directed many comments at the iron deposits themselves as their description and interpretation is reasonable. This review concentrates mostly on the sedimentological aspects of the manuscript, which are problematic. Basically not enough substantiating data is provided for the interpretations given. Many of the interpretations are very specific and the limited exposures available do not provide the types of data necessary to validate the interpretations. The author's interpretations, in general, could be correct, but there are other equally as valid interpretations of the depositional systems possible. This situation is not helped by the inclusion of references after an interpretation is put forward that describe a depositional process or rock unit that was formed in a similar environment to that proposed but appear to bear little in common with the rocks present in this study. This reduces down to the problem that the characteristics of the rocks described in this study are not detailed enough to support specific interpretations. For example: a conglomeratic unit is interpreted as a channelized mass flow deposit in a submarine fan. If it was deposited by a high-density turbidity current it will have certain internal characteristics that are well defined in the literature (see some of Walker and Lowe's older papers). If it was a debris flow it will have other characteristics, such as disorganized clast orientations, matrix support, poor sorting etc. that these conglomerates do not appear to have. However, there is an even bigger problem with this interpretation. Submarine fan channel successions form thick fining upwards successions, commonly over tens of meters vertically. Finally submarine fans are one category of submarine base of slope deposit, a group that also includes ramps and aprons, and no evidence is given why this would not be a ramp or an apron, or simply, and much more likely, a conglomerate bed. I put in the latter as a few conglomerate beds do not make a fan, ramp or apron, which are very much larger features. These are just the problems that exist with one interpretation of depositional environments. Similar problems exist with the others. It would have been beneficial if the authors delegated more discussion to the deposition of the silica-rich layers as the Fe-rich layers forming from hydrothermal fluids are easy to understand but the deposition of the silica layers in BIF is much more difficult to explain. The use of references is perplexing. Most of them do not have direct bearing on what they are referencing in the text. They are on the same general subject, but many do not reinforce the correctness of the preceding statement. I recommend that the

interpretations of the depositional environments of the siliciclastics be eliminated. They are very problematic and greatly distract from the manuscript.

**Response:** For the sake of clarity, we should indicate that we are not proposing the Milos BIF-type rocks as the exact equivalent of Precambrian BIFs or insinuating that the seawater in which they formed had the exact composition of the Precambrian oceans. But we have found several components of the deposit that have the potential of providing and aiding mechanistic models aimed at understanding how BIFs formed. They may give insights into the deep past from the present perspective? These are some of the challenges we wish to resolve by detailed description of the geological and geochemical processes behind the perplexing deposition of the Milos IF. To enable comparison, we use the simple definition of BIFs as marine sedimentary rocks with alternating layers of Fe-rich and Si-rich bands, containing at least 15% Fe. This definition does not restrict the potential for BIFs to form only in Precambrian oceans, although they are a major feature of this unique period, a time when seawater had extraordinarily high levels of dissolved Fe and Si.

What our data are showing is that these local conditions of elevated and cyclic supply of dissolved Fe and Si and accompanied by strict bottom water anoxic conditions in a localised reservoir cut off from the open ocean, can in principle allow the rare deposition of BIF-type rocks in the modern ocean. The rarity of these types of deposits in the present-day ocean hints that such conditions seldom develop under the existing atmosphere, but that they can indeed occur. Therefore we present these as a rare modern BIF-type facies, different from the Precambrian BIFs, in the same way the rare Neoproterozoic BIFs are different from the widespread Paleoproterozoic Superior BIFs, which are in turn distinct from the mainly Algoma-type Archean BIF deposits that are limited in scale. This paragraph has been edited and included in our conclusions to highlight the importance of distinguishing this deposit from the Precambrian formations.

We strongly agree that sedimentary features can be difficult to interpret with certainty. We have therefore reduced the degree to which these interpretations have been made for the above reasons laid down by this reviewer. We however believe that it is important to keep solid parts of the interpretations that help explain how anoxic conditions could have apparently developed in the CVSB to enable dissolved Fe enrichment and its oxidation to Fe(III). Further, sedimentology must not be interpreted independently from the geochemistry and redox. This has become even more crucial with the new Figure 13C-D that unambiguously supports the contentious anoxic depositional conditions previously illustrated by REEs. This new information has been acquired using the widely accepted iron extraction redox proxy (See Poulton, S.W. and Canfield, D.E. 2011. *Ferruginous conditions: A dominant feature of the ocean through Earth's history. Elements* 7, 107–112, for a review).

This reviewer indicates that it would have been more helpful to dedicate more time discussing the Si bands. Our data show that band formation was mainly controlled by the activity of Fe, while Si precipitation was a passive process that cannot be explored beyond the fact. As we have shown and discussed, it is the cyclic release and oxidation of ferrous Fe that in fact controls the enrichment of Fe in the Fe-rich bands and Si in the Si bands. This particular observation provides the first independent

modern verification for similar processes suggested to have formed the ancient BIFs (See Bekker et al. 2010 for details and references therein, cited in the main text).

The description and discussion of the IF can stand alone. Its lack of current formed structures implies a low energy environment and that is about all that can be inferred about physical processes from the IF. Thus, the manuscript would need major revisions. A more detailed line by line review follows:

**Response:** We agree with this reviewer about the low-energy environment in which the IF formed, which is in agreement with our initial conclusions. However, it would appear that the switch from one redox state to the other was often accompanied by tectonic activity that caused deepening and shallowing.

Line 73: Rare Earth Elements should not be capitalized.

**Response:** Corrected

Line 115: Rhyolite is not intrusive.

**Response:** Corrected to extrusive

Line 226: It is much more common in work on iron formations to use PAAS to normalize the data.

**Response:** The rationale for using the NASC is as follows:

1. The NASC normalization maintains data consistency with the REE data published in our previous papers on the Milos IF ((1) Chi Fru, E., Ivarsson, M., Kiliyas, S.P., Bengtson, S., Belivanova, V., Marone, F., Fortin, D., Broman, C., and Stampanoni, M.: Fossilized iron bacteria reveal a pathway to the origin banded iron formations. Nat. Comm., 4, 2050 DOI: 10.1038/ncomms3050, 2013. (2) Chi Fru, E., Ivarsson, M., Kiliyas, S.P., Frings, P.J., Hemmingsson, C., Broman, C., Bengtson, S. and Chatzitheodoridis, E.: Biogenicity of an Early Quaternary iron formation, Milos Island, Greece. Geobiology, 13, 225–44, 2015.
2. There are no scientifically demonstrated discrepancies between the PAAS and NASC.
3. Following the above suggestion, data was normalized to PAAS for comparison with the NASC normalized trends. The results produced the same trend as observed when data are normalized to NASC. See new Figure 14 in the manuscript text, accessible in the attached supplement PDF file. Further explanations are also provided under sections 2.6-2.6.1 in the manuscript supplement text.

Line 327: Below storm wave base does not necessarily mean below 100 to 200 meters. At present storm wave penetration is deepest in locations such as southeastern Australia and Atlantic Canada where it reaches 120m. But these are very storm prone open ocean facing areas. It is difficult to give an estimate for paleo-storm wave base in the study area, but I doubt that it could be even close to 100m as more would mean waves with greater than 200 meter wavelengths in a sheltered area compared to the open Atlantic.

**Response:** We have omitted our attempt at specifying a value in the text for the depth. The new wording has been rephrased to:

*The MFIF rests directly on the submarine dacites-andesites that were deposited in a relatively shallow submarine environment (Stewart and McPhie, 2006).*

Line 340: Not enough evidence is given to justify the turbidite interpretation. Graded beds just mean they were deposited by powering-down events, which can occur in many different environments. Even if they are turbidites, which I have no idea whether they are or not from the evidence, the setting cannot be termed a fan, ie, why not a ramp or apron or a number of other environments that can have turbidites.

**Response:** Removed from text.

Line 344: Slump deposits infers an intact or partially intact block that slid. The conglomerates are not slump deposits. They could be debris flows, but again there is not enough evidence given to say this.

**Response:** Lines 337-361 have been deleted and replaced with this short paragraph:

*In the overlying sandstone-conglomerate facies, the presence of sedimentary structures indicative of wave action and currents (e.g. cross-stratification), that signify rapid deposition during a high energy event, are consistent with a switch to a shallow-submarine high energy environment (Stewart and McPhie, 2006; Chi Fru et al., 2015). This shift in depositional environments may have been controlled by a combination of submarine volcano-constructional processes, synvolcanic rifting and volcano-tectonic uplift known to have formed the CVSB (Papanikolaou et al., 1990; Stewart and McPhie, 2006).*

Line 347: If a flow is carrying pebbles it is not a low density turbidity current.

**Response:** Deleted and replaced with the paragraph above.

372: gravel to pebble is not proper terminology. Pebbles are gravel if unconsolidated.

**Response:** Lines 370-373 have been deleted and replaced with:

*The lower sandstone facies represents the host of the main economic grade Mn oxide ores in the CVSB. This constitutes part of a separate study devoted to the Mn ores and will not be dealt with further here.*

Line 395: mm-scale layers are not beds, they are laminae.

**Response:** Deleted and replaced with laminations.

Line 418: Why not below storm wave-base?

**Response:** Corrected.



Line 422: The only evidence for the interpretation that the conglomerates are “ a series of channel deposits in an inner turbidite fan-like setting” appears to be that they are conglomerates. A great deal more evidence is necessary to be so specific about the depositional environment.

**Response:** Lines 420-434 have been deleted.

Line 424: No evidence has been given for a tidal environment and little evidence for a shoreface.

**Response:** Lines 420-434 have been deleted.

Line 427: There are also many papers that describe iron formations in other settings.

**Response:** Lines 420-434 have been deleted.

Line 434: This is an example of a reference that has little bearing on the preceding statement. The Mesoarchean Barberton is not a good analog for the sedimentary environment of the basin described here.

**Response:** Lines 420-434 have been deleted.

Line 439: The sedimentary structures described could have been formed in the environments proposed, but they are not limited to the environments given the lack of evidence.

**Response:** Lines 335-340 deleted.

Line 458: The description of these deposits has little in common with GIF. It is also better to reference the originator of the term GIF (Simonson), rather than Bekker, which is just a review article.

**Response:** References to GIF have been deleted from the text.

Line 481: This is circular reasoning.

**Response:** We agree and further demonstrate this in the new Figure 13D. These emphases must be highlighted to show some of the similarities these rare deposit shares with true BIFs.

Line 482: Precambrian BIF can be sulfide facies.

**Response:** We agree. We are trying to make the statement that these are those type of BIF facies that are sulfide rich. We have therefore replaced with the text:

*Lack of association of the framboidal-iron-rich particles with S, following SEM-EDS analysis, rules out a pyrite affiliation and is consistent with the non-sulfidic depositional model suggested by the sequential iron extraction redox proxy (Fig. 13D).*

Line 522: This statement is not correct. Planavsky and others (see authors' references to this statement) put forward that the anomaly for Ce must be less than .95 and greater than 1.05 to be significant, not less than or greater than 1.

**Response:** This has been corrected.

Line 528: They do not have similar enrichment levels; they are light depleted.

**Response:** Enrichment changed to depleted.

Line 574: The positive Eu anomalies are quite small compared to those associated with oceanic hydrothermal vent sediments. Also, volcanic detritus can carry positive Eu anomalies. A plot of Ti vrs Eu\* would be useful to distinguish if the anomaly is related to volcanic detritus in the IF.

**Response:** We agree, but this effort will not tell us anything more than what we have already shown, since multiple evidence shows that we are dealing with materials being released into the basin intermittently by hydrothermal/volcanic activity as demonstrated by the ash particles in the bands. As we have shown in Figure 13 and from using multiple lines of evidence, the supply of materials from the continent to the basin was not an important source of sediments during the formation of the alternating Fe and Si layers. Our main interpretation is a hydrothermal source, backed by data in our cited publication in Nature Communications and Geobiology, in addition to the present submission.

Line 614: What is described as an upward fining trend appears to me to be simply one single graded bed. The fining upwards in the bed is better explained by the depositional mechanism losing energy through time. Also, conglomeratic beds usually represent rapid deposition during a high energy event, ie. storm or mass flow, rather than the slow pebble on pebble accumulation over years.

**Response:** This text has been revised as suggested. The new text reads like this:

*Geomorphological/chemical reconfiguration orchestrated the deposition of the NFIF in a deeper, small-restricted basin (Fig. 2). The deepening of Basin 3 is reflected in the underlying graded conglomerate bed that exhibits an upward fining trend, followed by transition into the fine-grained NFIF. The conglomerate bed may represent rapid deposition during a high-energy event, i.e. storm or mass flow, whereas the upwards fining in the bed is better explained by the depositional mechanism losing energy through time. These high-energy conditions apparently must have ceased during the deposition of the overlying NFIF, where we interpret that increased abundance of finely laminated IF and decreased evidence of storm and/or mass flow reworking reflects deepening conditions. The hypothesized deepening of Basin 3 is consistent with the interpretation that active rifting was an important mechanism in the formation of the CVSB (Papanikolaou et al., 1990).*

Line 682: Comparing the small Eu anomalies present in this study with the larger Precambrian anomalies should include giving the values for the average Precambrian anomalies. Simply stating the values of Eu anomalies of samples in this study are more similar to Archean anomalies is somewhat misleading.

**Response:** The paragraph has been deleted.

Line 757: If even small amounts of seawater are mixing with the hydrothermal fluid, as previously stated, anoxia could not exist.

**Response:** See new Figure 13C-D that firmly establishes the anoxic/ferruginous depositional conditions. Moreover the statement made by this reviewer that even if small amounts of seawater are mixing with hydrothermal fluid, anoxia cannot exist, is misleading and a bit perplexing because this argument means that redox gradients should not exist in nature. Following the rules of stoichiometry in chemical reactions, large volumes of highly reduced solutions such as hydrothermal fluids require equally large concentrations of oxidants (especially oxygen) to make the fluid oxidizing. From this reasoning, considerable amounts of oxygen are required to react with the large volumes of the highly reduced chemicals and compounds present in hydrothermal fluids. This argument is given as an explanation for why it took so long for oxygen to rise in the atmosphere (See Lyons et al., 2014. The rise of oxygen in Earth's early ocean and atmosphere. *Nature* 506:307–315; and the review by Bekker et al. 2010, cited in the manuscript). The reasoning is that reduced hydrothermal fluids that made up a bulk of the early oceans were eventually overwhelmed stoichiometrically by oxygen (meaning more oxygen was being produced than consumed by the reduced fluids), leading to the rise of oxygen in the atmosphere, c. 2.4 billion years. Even after that, although the Paleoproterozoic surface ocean was oxidized for close to two billion years, complete ocean oxygenation only came at the end of the Precambrian despite the fact that reduced deep ocean hydrothermal fluids continuously mixed with the oxygen-rich ocean surface seawater. If we were to follow the argument given by this reviewer, then the whole ocean would have been oxidized following the mixing of the reducing fluids with the thin layer of oxygen-rich seawater on the ocean surface. This indicates that the sedimentology, geochemistry and redox must be jointly interpreted to understand what occurred at Milos.

Line 842: The presence of a conglomeratic bed does not commonly mean deepening of a marine succession. There are literally thousands of papers where the upward transition of sandstones to conglomerates is interpreted as shallowing as energy levels increase with shallowing in a marine setting.

**Response:** We strongly agree that the paragraph was not well-phrased, leading to the difficulty in understanding the meaning of the sentence. It has now been revised to:

*All of this is feasible with the three-basin-fault-bounded hypothesis as a requirement for movement along fault lines in response to temporal tectonic activation. The upward sequence transition from the Mn-rich sandstone facies, through the pebbly conglomerate and the final termination in the overlying mud-grained NFIF (Fig. 8B), reflect sedimentary features formed during multiple changes in seawater levels (Cattaneo & Steel, 2000). This study proposes that the NFIF that overlies the transgressive-type conglomeratic lag along an erosional contact surface was likely deposited during maximum flooding, when the basin became stagnant and stratified, and subsequently was uplifted to emergence.*

Line 848: The presence of a transgressive conglomeratic lag implies that the area was emergent prior to this and the conglomerate formed by wave reworking in a shore proximal environment. Evidence has not been given to support this, and if I am not mistaken the conglomerate has previously in this manuscript been interpreted as a mass flow.

**Response:** Deleted.

Line 853: In these references the maximum regressive surface is overlain by a transgressive lag and then very shallow shoreline deposits affected by wave activity. A very different scenario to what these authors are proposing.

**Response:** Paragraph and references removed.

Line 855: The referenced BIFs are not deposited in sandstone/grainstone environments, the IFs are grainstone with very low siliciclastic contents and they are interlayered with chemical muds, but the IFs are not banded.

**Response:** Because this interpretation is not of immediate relevance to the strength of the paper, the paragraph has been deleted.

Line 1004: This process would be expected to produce a sharp bottom contact to the Fe-rich layer, which would then mineralogical grade upwards into the silica-rich layer. Is this the way the layers are organized?

**Response:** Yes. We show this in supplementary Figures 8 and 9.

1  
2 Sedimentary mechanisms of a modern banded iron formation on  
3 Milos Island, Greece  
4

5 <sup>1,2</sup>Ernest Chi Fru\*, <sup>3</sup>Stephanos Kiliass, <sup>4,5</sup>Magnus Ivarsson, <sup>1</sup>Jayne E. Rattray,  
6 <sup>3</sup>Katerina Gkika, <sup>2</sup>Iain McDonald, <sup>6</sup>Qian He, <sup>1</sup>Curt Broman

7  
8 <sup>1</sup>Department of Geological Sciences, 10691, Stockholm University, Sweden.

9 <sup>2</sup>School of Earth and Ocean Sciences, Cardiff University, Park Place, CF10 3AT,  
10 Cardiff, UK.

11 <sup>3</sup>Department of Economic Geology and Geochemistry, Faculty of Geology and  
12 Geoenvironment, National and Kapodistrian University of Athens, Panepistimiopolis,  
13 Zographou, 15784, Athens, Greece.

14 <sup>4</sup>Department of Biology, University of Southern Denmark, Campusvej 55, Odense M,  
15 DK5230, Denmark

16 <sup>5</sup>Department of Palaeobiology, Swedish Museum of Natural History, Box 50007,  
17 Stockholm, Sweden.

18 <sup>6</sup>School of Chemistry, Cardiff University, Park Place, CF10 3AT, Cardiff, UK.

19  
20 \*Corresponding author

21 Tel: +44(0) 29 208 70058

22 Email: ChiFruE@cardiff.ac.uk  
23  
24

25

26 Short title: A modern banded iron formation

27 **Abstract.** An Early Quaternary shallow submarine hydrothermal iron formation (IF)  
28 in the Cape Vani sedimentary basin (CVSB) on Milos Island, Greece, displays banded  
29 | rhythmicity similar to Precambrian banded iron formation (BIF). [Sedimentary and](#)  
30 stratigraphic reconstruction, coupled to biogeochemical analysis and micro-nanoscale  
31 mineralogical characterization, confirm the Milos IF as a modern BIF analogue.  
32 Spatial coverage of the BIF-type rocks in relation to the economic grade Mn ore that  
33 brought prominence to the CVSB implicates tectonic activity and changing redox in  
34 their deposition. Field-wide stratigraphic and biogeochemical reconstruction  
35 demonstrate two temporal and spatially isolated iron deposits in the CVSB with  
36 distinct sedimentological character. Petrographic screening suggests the previously  
37 described photoferrotrophic-like microfossil-rich IF (MFIF), accumulated on  
38 basement andesite in a ~150 m wide basin, in the SW margin of the basin. A strongly  
39 | banded non-fossiliferous IF (NFIF) [sits on top](#) the Mn-rich sandstones at the transition  
40 to the renowned Mn-rich formation, [capping the NFIF unit](#). Geochemical evidence  
41 relates the origin of the NFIF to periodic submarine volcanism and water column  
42 oxidation of released Fe(II) in conditions apparently predominated by anoxia, similar  
43 to the MFIF. Raman spectroscopy pairs hematite-rich grains in the NFIF with relics of  
44 a carbonaceous material carrying an average  $\delta^{13}\text{C}_{\text{org}}$  signature of ~-25‰. However, a  
45 similar  $\delta^{13}\text{C}_{\text{org}}$  signature in the MFIF is not directly coupled to hematite by  
46 mineralogy. The NFIF, which post dates large-scale Mn deposition in the CVSB, is  
47 composed primarily of amorphous Si (opal-SiO<sub>2</sub>·nH<sub>2</sub>O) while crystalline quartz  
48 (SiO<sub>2</sub>) predominates the MFIF. An intricate interaction between tectonic processes,  
49 changing redox, biological activity and abiotic Si precipitation [are proposed to have](#)  
50 [collectively](#) formed the unmetamorphosed BIF-type deposits [in a shallow submarine](#)  
51 [volcanic center](#).

52

53

54

55

56 **Keywords:** Banded iron formation; BIF analogue; Hydrothermal activity; Iron

57 cycling; Silica cycling.

58

59

60

61

62

63

64

65

66

67

## 1 Introduction

[Banded iron formations \(BIFs\)](#), are marine sedimentary deposits containing at least 15% Fe, marked by Fe-rich bands alternating with Si-rich layers that formed predominantly during the Precambrian (James, 1954; Gross, 1980; Simonson, 1985, 2003; Bekker et al., 2010). Recently, an Early Quaternary iron formation (IF), ~2.0 million years old, displaying banded rhythmicity typical of Precambrian banded iron formations (BIF) was serendipitously discovered in the Cape Vani sedimentary basin (CVSB) on Milos Island, Greece (Chi Fru et al., 2013, 2015). Before this discovery, Cape Vani was long known to host Mn oxide ores of economic potential (Hein et al., 2000; Liakopoulos et al., 2001; Glasby et al., 2005; Kiliass et al., 2007). Milos is an emergent volcano on the Hellenic Volcanic Arc (HVA) where arc-volcanism and seafloor hydrothermal activity occur in thinned pre-Alpine to Quaternary continental crust (Kiliass et al., 2013b) (Fig. 1). The first reported IF from Cape Vani is unmetamorphosed and contains diverse microfossils encrusted by hematite, with ferrihydrite proposed as a primary precursor mineral (Chi Fru et al., 2013, 2015). Field stratigraphy, rare earth elements (REEs), stable isotopes, petrographic and microfossil studies point to microbial Fe deposition in a semi-enclosed, shallow submarine basin under conditions analogous to those that formed the Precambrian Algoma-type BIFs near volcanic centers (Chi Fru et al., 2015). These earlier reports assumed a one-time basin-wide depositional event and a common origin for all Fe-rich sedimentary rocks in the CVSB.

However, it remains unclear what sedimentary processes caused the distinct deposition of the BIF-type rocks in a basin where Mn precipitation was apparently widespread at various intervals. Moreover, it is not known how the Mn ores relate temporally and spatially to Fe deposition in the ~1 km long CVSB. This knowledge



may provide clues to processes that triggered large-scale deposition of similar Proterozoic Fe-Mn-rich deposits (Roy, 2006; Tsikos et al., 2010; [Beukes et al., 2016](#)). Here, new sedimentological, petrological and biogeochemical evidence describes cycles of periodic precipitation of shallow submarine Si and Fe-rich sedimentary rocks and the plausible mechanisms that enabled their temporal and spatial separation from the Mn deposits in the CVSB. The data reveal a much more complex depositional system not only controlled by microbial Fe(II) oxidation as previously proposed (Chi Fru et al., 2013, 2015), but illuminates episodic submarine hydrothermal activity coupled to changing redox conditions as a central mechanism in the formation of the banded iron rocks.

## 1.1 Geological setting

K-Ar radiometric dating of biotite and amphiboles belonging to the dacitic/andesitic lava domes flooring the CVSB basin gave an Upper Pliocene age of  $2.38 \pm 0.1$  Ma (Fytikas et al., 1986; Stewart and McPhie, 2006). The fossiliferous sandstones/sandy tuffs hosting the Mn-rich deposit, which contain the gastropod mollusk guide fossil, *Haustator biplicatus* sp. (Bronn, 1831), indicate an Upper Pliocene-Lower Pleistocene age. The geology, Fe and Mn mineralization of the CVSB have previously been described in detail (Plimer, 2000; Hein et al., 2000; Liakopoulos et al., 2001; Skarpelis and Koutles, 2004; Glasby et al., 2005; Stewart and McPhie, 2006; Kiliadis, 2011; Alfieris and Voudouris, 2005; Alfieris, 2006; Alfieris et al., 2013; Chi Fru et al., 2013, 2015; Papavassiliou et al., 2017). Briefly, the Milos IF is part of the CVSB, a recently emergent sedimentary rift basin located NW of Milos Island, along the HVA in the Aegean Sea, Greece (Fig. 1). It hosts a fossil analogue of active shallow-submarine hydrothermal activity on the coast of Milos Island (Dando et al., 1995).

The CVSB developed within a shallow-submarine rhyolitic-dacitic volcanic center, filled up mainly by a ~35-50 m thick stratigraphic succession of volcanoclastic/epiclastic sandstones and sandy tuffs spanning Upper Pliocene to Lower Pleistocene, 35-40% of which is hydrothermally mineralized by Mn oxides and barite (Hein et al., 2000; Liakopoulos et al., 2001; Skarpelis and Koutles, 2004; Papavassiliou et al., 2017). Sedimentologic and ichnologic data, including sedimentary structures, lamellibranch, echinoid and brachiopod fossils, the gastropod mollusk fossil, *Haustator biplicatus* (Bronn, 1831), and microbially induced sedimentary structures (e.g., Kiliass, 2011), suggest that most of the CVSB sandstones/sandy tuffs hosting the Mn-rich deposit, are foreshore to shoreface shallow submarine deposits, formed at a maximum depth of 200 mbsl. Over the last 0.8 Myr, fluctuating water depths due to sea-level change of up to 120 m and volcanic edifice building, has resulted in tectonic uplift of ~250 m (Papanikolaou et al., 1990). The CVSB infill, currently 35 m above sea level, is tectonically bound by [extrusive rhyolite to the north](#), framed by elevated andesitic-dacitic centres, with the Cape Vani and the Katsimoutis dacitic lava domes being the most prominent (Fig. 1).

## 2 Methodology

### 2.1 Sample preparation

Prior to mineralogical and geochemical analysis, exposed rock surface layers were sawn and removed. GeoTech Labs (Vancouver, Canada) produced doubly polished thin sections for mineralogical and textural analysis. [Trace and rare earth elements analysis](#) was performed on pulverized powders [digested with a mixture of HNO<sub>3</sub>, HF and heat until a clear solution was obtained](#) (Chi Fru et al., 2013, 2015).

## 143    **2.2 Mineralogical analysis**

### 144    **2.2.1 X-Ray Diffraction (XRD) analysis**

145    A PANalytical Xpert-pro diffractometer at room temperature, 45 kV, 40 mA and  
146    1.5406 Å wavelength and Cu-K $\alpha$  radiation and Ni-filter, was used for Powder X-Ray  
147    Diffraction (PXRD) analysis. Samples were analyzed between 5-80° in step sizes of  
148    0.017° with continuous mode scanning step time of 50.1650 s while rotating.

149

### 150    **2.2.2 Raman spectroscopy**

151    Raman analysis was performed with a confocal laser Raman spectrometer (Horiba  
152    instrument LabRAM HR 800), equipped with a multichannel air-cooled (-70°C) 1024  
153    x 256 pixel charge-coupled device (CCD) array detector as previously described (Chi  
154    Fru et al. 2013, 2015). Spectral resolution was ~0.3 cm<sup>-1</sup>/pixel. Accuracy was  
155    determined by a repeated silicon wafer calibration standard at a characteristic Raman  
156    line of 520.7 cm<sup>-1</sup>.

157

### 158    **2.2.3 Transmission electron microscopy**

159    Specimens for transmission electron microscopy (TEM) were prepared from the  
160    crushed rock specimen powder. This was followed by dry-dispersal onto a 300 mesh  
161    holey carbon TEM Cu grid. Microscopy was conducted using a JEOL 2100 TEM  
162    with a LaB<sub>6</sub> source in the School of Chemistry, Cardiff University, operated at  
163    200kV. The X-EDS analysis was performed with an Oxford Instrument SDD detector  
164    X-Max<sup>N</sup> 80 T.

165

### 166    **2.2.4 Scanning electron microscopy**

Scanning Electron Microscopy-Energy Dispersive Spectroscopy (SEM-EDS) analysis was done on a FEI QUANTA FEG 650 ESEM. Images were captured at 5 kV and EDS data collected at 20 kV, using an Oxford T-Max 80 detector (Oxford Instruments, UK). The analyses were performed in low vacuum to minimize surface charging of uncoated samples. EDS elemental maps were collected for 30 min or until the signal had stabilized, indicated by a clear distribution trend. The data were further processed with the Oxford Aztec software.

## **2.3 Geochemical analysis**

### **2.3.1 Laser ablation ICP-MS and trace element analysis**

Laser Ablation-Inductively Coupled Plasma-Mass Spectrometry (LA-ICP-MS) was performed at Cardiff University on polished thin sections. The LA-ICP-MS system comprised a New Wave Research UP213 laser system coupled to a Thermo X Series 2 ICP-MS. The laser was operated using a frequency of 10 Hz at pulse energy of ~5mJ for an 80µm diameter beam using lines drawn perpendicular to the layering and at a movement speed of 26 microns sec<sup>-1</sup>. Samples were analyzed in time resolved analysis (TRA) mode using acquisition times of between 110 and 250 seconds; comprising a 20 second gas blank, 80-220 second ablation and 10 second washout. Dwell times varied from 2 msec for major elements to 35 msec for low abundance trace elements. Blank subtraction was carried out using the Thermo Plasmalab software before time resolved data were exported to Excel.

Separated and independently pulverized banded layers were digested by lithium borate fusion followed by major, trace and rare earth element (REE) analyses using ICP- [Atomic Emission Spectrometry-Mass Spectrometry \(ICP-AES-MS\)](#) and [X-Ray Fluorescence \(XRF\)](#) at [Bureau Veritas \(Ankara\)](#). Geochemical data were compared

with previously published results for the more widely investigated Mn deposits (Hein et al., 2000; Liakopoulos et al., 2001; Glasby et al., 2005).

### 2.3.2 Isotope analysis

C, N and S isotopic composition for the pulverized samples was determined as previously described (Chi Fru et al., 2013, 2015), following combustion in a Carlo Erba NC2500 analyzer and analyzed in a Finnigan MAT Delta V mass spectrometer, via a split interface to reduce gas volume. Reproducibility was calculated to be better than 0.15‰ for  $\delta^{13}\text{C}$  and  $\delta^{15}\text{N}$  and 0.2‰ for  $\delta^{34}\text{S}$ . Total C and N concentrations were determined simultaneously when measuring the isotope ratios. The relative error was <1% for both measurements. For carbon isotopic composition of organic carbon, samples were pre-treated with concentrated  $\text{HNO}_3$  prior to analysis.

### 2.4 Organic geochemistry analysis

Lipid biomarker and compound specific  $\delta^{13}\text{C}$  analyses were executed on powdered samples of sectioned bands from which exposed surface layers had been removed. Modern sediments from Spathi Bay, 36°40'N, 24°31'E, southeast of Milos Island, collected by push coring at 12.5 m below the seafloor were freeze-dried prior to extraction to aid the identification of potential syngenetic biomarkers in the Quaternary rocks. Between 4-6 g of ground samples were ultrasonically extracted using 3×Methanol, 3×(1:1) Methanol:Dichloromethane (DCM), and 3×DCM and extracts were combined and dried under  $\text{N}_2$ . Samples were subsequently re-dissolved in DCM then methylated following the method of Ichihara and Fukubayashi (2010).

The resulting residue was silylated using, 20  $\mu\text{l}$  pyridine and 20  $\mu\text{l}$  [\(N, O-Bis\(trimethylsilyl\)trifluoroacetamide\)](#) BSTFA and heated at 60°C for 15 min. Total

lipid extracts were analyzed using a Shimadzu QP 2010 Ultra gas chromatography mass spectrometer (GC/MS). Separation was performed on a Zebtron ZB-5HT column (30 m x 0.25 mm x 0.10  $\mu$ m) with a helium carrier gas flow at 1.5 ml min<sup>-1</sup>. Samples were injected splitless, onto the column at 40°C with the subsequent oven temperature program ramped to 180°C at a rate of 15°C min<sup>-1</sup>, followed by ramping to 325°C at a rate of 4°C min<sup>-1</sup> and a final hold for 15 min. The MS was set to scan from 50 to 800 m/z with an event time of 0.70 sec and a scan speed of 1111 u/sec. All peaks were background subtracted and identification confirmed using the NIST GC/MS library and literature spectra. Contamination was not introduced into the samples, as blank samples worked up concurrently with the rock fractions had results comparable to the ethyl acetate instrument blank.

## 2.5 Chemical weathering analysis

Chemical index of alternation (CIA) was used to determine whether variations in chemical weathering intensities would in addition to hydrothermal activity deliver materials into the depositional basin from the continent, according to the formula:  $CIA = Al_2O_3 / (Al_2O_3 + CaO + Na_2O + K_2O) \times 100$ . Extensively applied, the CIA index reveals subtle changes in weathering fluxes (Nesbit and Young, 1982; Maynard, 1993; Bahlburg & Dobrzinski, 2011), where increasing CIA values generally indicate amplified chemical dissolution of rocks and selective release of dissolvable CaO, Na<sub>2</sub>O and K<sub>2</sub>O into solution (Nesbit & Young, 1982; Maynard, 1993; Bahlburg & Dobrzinski, 2011). The broken rock particles enriched in the poorly soluble Al<sub>2</sub>O<sub>3</sub> fraction, settle to the seafloor as weathered sediments carrying a chemical composition different from the source. In the absence of chemical dissolution, no net chemical change is expected in the composition of sediments

compared to source and thus a low CIA index. CIA indices for detritus of 0-55, 55-75 and >75, are considered unweathered, unweathered to slightly weathered and weathered to highly weathered, respectively (Nesbit & Young, 1982; Maynard, 1993; Bahlburg & Dobrzinski, 2011).

## **2.6 Redox analysis**

Redox depositional conditions were evaluated using the sequential Fe extraction redox proxy (Poulton and Canfield, 2005, 2011), combined with REE composition of the sediment (Planavsky et al., 2010).

### **2.6.1 REE redox analysis**

REE data obtained as described in section 2.3.1 were normalized with the North American Shale Composite (NASC) to maintain consistency with previous studies in which NASC-normalized REE data (SN) were reported for the Milos BIF-type rocks (Chi Fru et al., 2013, 2015). The data were further normalized with the Post Archean Australian Shale (PAAS) (McLennan, 1989) standard for comparative purposes, according to Bau and Dulski (1996). Ce anomalies, calculated from  $Ce/Ce^*$  ( $Ce_{(SN)}/0.5Pr_{(SN)} + 0.5La_{(SN)}$ ) and  $Pr/Pr^*$  ( $Pr_{(SN)}/0.5Ce_{(SN)} + 0.5Nd_{(SN)}$ ) values, were considered significant when  $Ce/Ce^*$  and  $Pr/Pr^*$  were less than and greater than 1, respectively (Bau and Dulski et al., 1996; Planavsky et al., 2010).

### **2.6.2 Sequential iron extraction redox analysis**

This analysis was performed on three representative MFIF samples and the six sectioned bands of a typical NFIF sample using the method developed by Poulton and Canfield (2005) and data interpreted accordingly (e.g., Canfield and Poulton, 2005,



267 2011; Guilbaud et al. 2015; Sperling et al. 2015). Reagent blanks and geological  
268 standards were used for data calibration.

269

## 270 **3 Results**

### 271 **3.1 Lithostratigraphy**

272 **Sedimentary structures, grain-size trends, lateral facies variations, vertical stacking**  
273 **trends, and key stratigraphic surfaces form the basis for facies analysis.** Field-wide  
274 sedimentological and lithostratigraphical mapping of the CVSB in the summer and  
275 fall of 2014 enabled the assessment of the lateral and vertical coverage of the Milos  
276 iron oxide-rich facies relative to the Mn-rich sandstones that dominate the Early  
277 Quaternary sedimentary basin (Fig. 2). Six stratigraphic sections, representing marine  
278 siliciclastic lithofacies sequences, were investigated along a ~1 km SW-NE trending  
279 portion of the CVSB infill (Supplementary Figs 1-7). Sequence stratigraphy was  
280 conducted on outcrops and vertical shafts and tunnels left behind by previous Mn  
281 mining activity. Two of those sections; Section A located at 36°44'17.85''N,  
282 24°21'17.72''E and Section B located at 36°44'35.11''N, 24°21'11.25''E, contain  
283 stratigraphic units composed of layered, bedded, or laminated rocks that contain  $\geq 15$   
284 % Fe, in which the Fe minerals are commonly interlayered with quartz or chert, in  
285 agreement with the definition of Precambrian BIFs (James, 1954; Gross, 1980;  
286 Bekker et al., 2010). These IFs are descriptively referred to here as microfossiliferous  
287 iron formation (MFIF) according to Chi Fru et al. (2013, 2015), and non-  
288 microfossiliferous iron formation (NFIF) (this study), respectively (Fig. 2). The MFIF  
289 and the NFIF occupy at most ~20% of the entire CVSB infill. The stratigraphy and  
290 sedimentary lithofacies are illustrated below, using lithofacies codes modified after

291 Bouma (1962), Miall (1978, 1985), Lowe (1982), Mutti (1992) and Shanmugam  
292 (2016).

293 Further field stratigraphic survey revealed considerable lithologic variability  
294 within three fault-bounded volcanosedimentary sub-basins in the CVSB (Fig. 2),  
295 which for the sake of simplicity are referred to as Basin 1—host of the MFIF; Basin  
296 2—host of economic grade Mn ore; and Basin 3—host of the NFIF (Fig. 2). Each  
297 section is framed by distinct marginal normal faults that strike in the NW-SE and NE-  
298 SW to NNE-SSW directions, distinguishable by distinct lateral sedimentary facies  
299 exhibiting unique vertical sequence stratigraphy (Fig. 2; Supplementary Figs 1-7).  
300 Faulting in the CVSB is related to major geographical activation of extensional  
301 structures at intervals that shaped Milos into a complex mosaic of neotectonic units  
302 (Papanikolaou et al., 1990; van Hinsbergen et al., 2004).

303

#### 304 **3.1.1 Section A (36°44'17.85"N, 24°21'17.72"E)**

305 Informally known as “Little Vani”, Section A is the type section containing the MFIF  
306 at the base. It crops out in the W-SW edge of the CVSB (Figs 1 & 2) as a ~6-7 m high  
307 cliff resting stratigraphically on submarine dacitic and andesitic lavas and domes.  
308 This section extends laterally in the N-NE direction for an estimated 300–500 m.

309 | Lithologically, the MFIF comprises laminated and massive fine-grained red  
310 and white weathered ferruginous jaspelitic red chert layers (Chi Fru et al., 2013,  
311 2015). The chert layers contain morphologically distinct Fe minerals dispersed in a  
312 fine-grained siliceous matrix (Fig. 3), marked by the notable absence of pyrite and an  
313 extremely low S content (Chi Fru et al., 2013, 2015). Layers are tabular and typically  
314 laterally continuous at scales of several meters, whereas wave and current structures  
315 (e.g., cross-lamination) are generally absent from the MFIF. The hematite-rich MFIF

Ernest C 26/2/2018 20:27

**Deleted:** The MFIF is correlatively interpreted to be in direct stratigraphic contact with Late Pliocene-Early Pleistocene (2.5–1.5 Ma) basement submarine dacitic-andesitic rocks.

321 laminae (Table 1) are built by massive encrustation of anoxygenic photoferrotrophic-  
322 like microbial biofilms by precipitated Fe (Chi Fru et al., 2013). The base of the MFIF  
323 outcrop, is visibly mineralized by black diffused bands/veins composed of Mn oxides  
324 (Fig. 4 & Table 1).

325 | A markedly ferruginous 2-3 m-thick section immediately overlies the MFIF,  
326 comprising a distinct package of Fe-rich beds that transition up the section (Figs 4A  
327 & 5). The lower 1-2 m consist of fine-grained sandstone beds that are well to  
328 moderately sorted, containing a 20-40 cm thick portion dominated by plane parallel-  
329 laminated sandstone/sandy tuff, massive to plane parallel-laminated sandstone/sandy  
330 tuff, and massive sandstone/sandy tuff lithofacies (Fig. 5; Supplementary Fig. 1). The  
331 fabric of these Fe-rich sandstone facies consists of sub-angular to sub-rounded and  
332 100–600 µm fine to medium-grained volcanoclastic K-feldspar grains, making up to  
333 75% of the total rock, with variable amounts of quartz and clay mineral grains.

334 The latter are overlain by a ~1-1.5 m sequence of poorly-sorted tabular clast-  
335 supported pebble-to-cobble conglomerate beds with an erosional base, grading  
336 | upward into coarse to medium-grained sandstone/sandy tuff beds, with alternating  
337 conglomerate cycles (Fig. 5), averaging 20-40 cm in thickness. The cobble/pebble  
338 conglomerate clasts include intraformational volcanic rocks (dacite, andesite),  
339 allochthonous volcanoclastic sandstone, and volcanoclastic microclasts (e.g. K-  
340 feldspar), cemented by hematite (Fig. 5; Chi Fru et al., 2013; Kiliash et al., 2013a).  
341 Towards the westernmost edge of the “Little Vani” section, there is a facies change  
342 from the graded pebbly conglomerate/sandy tuff rhythms to a predominantly Fe-rich  
343 | conglomerate bed (Fig. 6A), termed the conglomerate-hosted IF (CIF) in Chi Fru et  
344 al. (2015), with a maximum thickness of ~0.5 m and a cobble size range of ~10 cm.  
345 The Fe-rich conglomerate bed transitions upward into medium-grained pebbly reddish

ferruginous sandstones with thin volcanic rock and sandstone pebble lenses. This<sub>3</sub> in turn<sub>3</sub> grades upwards into a very-fine-grained greenish glauconite-bearing plane parallel-laminated sandstone to siltstone bed; characterized by soft-sediment deformation structures, such as flame structures, convolute bedding and lamination structures, loop bedding, load casts, and pseudonodules (Supplementary Figs 1-2).

The “Little Vani” section is eventually capped along an erosional surface by an overlying 1-2 m thick section dominated by medium to fine-grained and moderately to poorly-sorted reddish Fe-rich tabular sandstone beds, 10–40 cm thick, topped by patchy sub-cm to cm-thick Mn-rich sandstones (Fig. 5; Supplementary Figs 1-2). Dominant lithofacies of the Fe-rich sandstone cap include planar and hummocky cross-bedding, exhibiting bioturbation in places. The Fe-rich lithofacies cap is laterally discontinuous, thinning out basinwards towards the N-NE, and can be observed smoothly grading into a 1-2 m thick section composed of cm to sub-cm-thick Mn-rich volcanoclastic sandstone lithofacies, described below in Section B. No Fe-rich hydrothermal feeder veins are obvious in the MFIF. However<sub>3</sub> feeder veins and Mn horizons can be observed to truncate laminations in the MFIF, and up through the whole “Little Vani” section (e.g., Figs 4C & 5).

The MFIF rests directly on the submarine dacites-andesites that were deposited in a relatively shallow submarine environment (Stewart and McPhie, 2006). The fine-grained, finely laminated nature of the MFIF, and, the lack of evidence of current or wave structures (e.g., symmetric ripples or hummocky cross-stratification), coupled to the absence of volcanogenic detrital particles and intraclast breccia structures, indicate a low energy sedimentation environment, marked by negligible volcanic interference (e.g., Tice and Lowe, 2006; Konhauser et al., 2017). This interpretation is supported by the observed enrichment of Fe in the MFIF; a

characteristic of relatively deeper water lithofacies (Konhauser et al., 2017). This view is compatible with the proposition that hematite enrichment in the MFIF was under the control of photoferrotrophic biofilms (Chi Fru et al., 2013) known to thrive at lower light intensities (Kappler et al., 2005; Li et al., 2013; Konhauser et al., 2017). The quiet environmental conditions would have ensured the formation of such stable photoferrotrophic biofilms over extended periods of time that would have facilitated the oxidation of hydrothermally released Fe(II) and the deposition of Fe(III) minerals.

In the overlying sandstone-conglomerate facies, the presence of sedimentary structures indicative of wave action and currents (e.g. cross-stratification), that signify rapid deposition during a high energy event, are consistent with a switch to a shallow-submarine high energy environment (Stewart and McPhie, 2006; Chi Fru et al., 2015). This shift in depositional environments may have been controlled by a combination of submarine volcano-constructional processes, synvolcanic rifting and volcano-tectonic uplift known to have formed the CVSB (Papanikolaou et al., 1990; Stewart and McPhie, 2006).

### 3.2 Section B (36°44'35.11"N, 24°21'11.25"E)

This ~8-10 m thick fault-bounded stratigraphic section, here referred to as "Magnus Hill", is the type section that contains the NFIF (Figs 2 & 7; Supplementary Figs 3-4). Two lithostratigraphic units—a lower unit A and an upper unit B—are identified in this study. Unit A is made up of a lower sandstone facies that is ~4-5 m thick, dominated by a Mn-oxide cement, overlain by reddish brown Fe-rich massive sandstone beds (Fig. 8 & Supplementary Figs 3-4). The lower sandstone facies represents the host of the main economic grade Mn oxide ores in the CVSB. This constitutes part of a separate study devoted to the Mn ores and will not be dealt with

Ernest Chi Fru 22/2/2018 09:18

**Deleted:** The overlying lithofacies sequence record a switch to faster accumulation of volcanoclastic turbidites on the quiet MFIF deposit, with the fine, medium to coarse-grained sandstone lithofacies typifying deposition during low and high density turbiditic flows in the middle to inner parts of a turbidite fan-like environment (Lowe, 1982; Mutti 1992; Talling et al., 2012; Orme and Laskowski, 2016; Shanmugam, 2016; Wang et al., 2017). Massive conglomerates containing both allochthonous sandstone clasts and intraformational andesite-dacite are interpreted as channelized submarine debris flows or slump deposits sourced from adjacent topographic highs (Lowe, 1982; Stewart and McPhie, 2006; Orme and Laskowski, 2016). Also, deposition from a waning low density turbidity current is indicated by the upward fining bed of pebbly Fe-rich sandstone, greenish glauconite bearing sandstone and laminated siltstone. Up section, the abundance of parallel and cross stratified Fe-rich and Mn-rich sandstone facies along an erosional surface, reflect a change in deposition to a high energy, shallow submarine shoreface/foreshore setting, above a wave base.

... [1]

425 | [further here](#). Unit B, ~5 m thick, unconformably overlies unit A and comprises two  
426 | distinct packages of beds that transition up section from brownish pebble  
427 | conglomerate layers (0.5-1.0 m thick), in contact with the very fine-grained NFIF  
428 | deposit (Supplementary Fig. 8 & 9). The NFIF is capped by patchy cm-thick  
429 | crustiform Mn oxides. Bifurcating feeder veins composed of barite, quartz and Mn-  
430 | /Fe-oxide minerals cut through the underlying sandstone beds (Supplementary Fig. 4).

431 | [The NFIF is composed of strongly banded Fe-rich rocks \(Fig. 7\) exposed on the](#)  
432 | topmost part of “Magnus Hill”. About 2-3 m thick, the NFIF consists of mm to sub-  
433 | mm thick, dark grey and brown Fe-rich bands, interbanded with reddish brown Si-rich  
434 | layers (Figs 7 & 9-11; Supplementary Figs 10-11). Sedimentary structures in the  
435 | NFIF are predominantly characterized by rhythmic mm to sub-mm thick [laminations](#)  
436 | (e.g., Fig. 7). The iron oxide-rich bands made up mainly of hematite (Table 1 & Fig.  
437 | 10C) are typically composed of very fine-grained angular to sub-angular volcanic dust  
438 | material (i.e., fine volcanic ash with particle size under 0.063 mm, K-feldspar,  
439 | tridymite and cristobalite (Table 1) in an amorphous Si and crystalline hematite  
440 | matrix (Fig. 12)). The predominantly amorphous Si-rich bands are typically [planar](#),  
441 | finely laminated and composed of microcrystalline to cryptocrystalline ferruginous  
442 | chert.

443 | The NFIF is directly overlain by a ~1 m thick laminated to massive well-  
444 | indurated, nodular-pisolitic ironstone bed (Fig. 8A, C & D) that locally preserves a  
445 | sub-horizontal fabric reflecting the bedding in the original sediment or contain various  
446 | ferruginous clasts such as fragments, nodules, pisoliths, and ooliths set in a hematite-  
447 | rich siliceous matrix (Fig. 8C). Scattered cm scale pisoliths display a crude concentric  
448 | internal layering, characterized by open and vermiform voids filled by cauliflower-  
449 | like Mn oxides overprint (Fig. 8D). [The ferruginous NFIF lithofacies are interpreted](#)

Ernest Chi Fru 22/2/2018 09:28

**Deleted:** Sandstone beds are moderately to well-sorted and 5-15 cm thick, and Mn-mineralized lithofacies include plane parallel-laminated sandstone, plane parallel laminated to rippled sandstone, planar cross-bedded sandstone, and massive sandstone. Secondary lithofacies include thinly bedded (1-5 cm thick) greenish glauconite-bearing heterolithic sandstone and thin (< 5 cm thick) white to pale-brown sandy tuff beds interbedded with the other Lithofacies. The sandstone facies host the main economic grade Mn oxide ores in the CVSB, which typically construct texturally diverse cements associated with a variety of volcanoclastic detritus (i.e., K-feldspar, lithic fragments, altered volcanic glass, quartz, sericitized plagioclase, chloritized biotite) and authigenic barite and/or glauconite. This constitutes part of a separate study devoted to the Mn ores and will not be dealt with further here, as the focus of the current study is on the IFs. Kilias (2011), however, suggested that many of the sedimentary structures identified within the Mn-mineralized sandstone lithofacies are associated with microbial mat growth.

to represent the deepest water deposits in the “Magnus Hill” section based on its very fine-grained sedimentary composition, fine laminations and a paucity of intraclast breccias. These, combined with the lack of evidence for wave and current-formed sedimentary structures (e.g., hummocky cross-stratification, trough, ripple cross-stratification, and erosional contacts), indicate quiet water low energy sedimentation, likely below wave base (Simonson and Hassler, 1996; Trendall, 2002; Krapež et al., 2003; Konhauser et al., 2017).

We interpret that each graded Fe oxide-rich band of the NFIF (Supplementary Fig. 9), represents an individual fallout deposit from a proximal pyroclastic eruption. This interpretation is supported by normal grading in fine volcanic ash content that reflects their likely origin as pyroclastic fallout deposits in an otherwise quiet water setting. For example, tridymite is a stable SiO<sub>2</sub> polymorph formed at low pressures of up to 0.4 GPa and at temperatures of ~870-1470 °C (Swamy et al., 1994; Morris et al., 2016). The coincidence of tridymite formation with silicic volcanism is in agreement with the widespread distribution of andesite, dacite and rhyolite lava domes in the CVSB. For example, vapour phase production of tridymite together with sanidine identified in this study (Fig. 10) and Fe oxides is principally associated with rhyolite ash flow (Breitkreuz, 2013; Galan et al., 2013). Similarly, Cristobalite is a SiO<sub>2</sub> polymorph associated with high temperature rhyolitic eruptions (Horwell et al., 2010). Finally, in situ carbonaceous laminations are absent, suggesting that benthic microbial mat growth had no influence on deposition of the NFIF. Ironstones overlying the NFIF are difficult to interpret with the existing data, but may represent supergene ferruginous duricrust formation resulting from subaerial weathering (Anand et al., 2002).

Ernest Chi Fru 22/2/2018 09:31

**Deleted:** (e.g., Trower and Lowe, 2016, and references therein)

Ernest Chi Fru 22/2/2018 09:33

**Deleted:** This interpretation is consistent with (1) up section lithofacies change from predominantly sandstone facies of the lower unit to conglomerate facies (Fig. 8B), probably related to a series of channel deposits in an inner-turbidite fan-like setting (Orme and Laskowski, 2016). This sedimentary sequence shows overall deepening from a tidal to shoreface zone depositional environment to an offshore zone during periods of high sea level stand (Trower and Lowe, 2016); (2) conclusions of previous workers suggest that lithofacies with Fe-rich composition similar to the NFIF, were deposited from seawater in a basinal settings (Lowe and Byerly, 1999; Tice and Lowe, 2006). The hypothesized deepening of the “Magnus Hill” section is generally consistent with the interpretation that active rifting was occurring during the filling of the CVSB (Papanikolaou et al., 1990; Stewart and McPhie, 2006; Liakopoulos et al., 2001; Papavassileiou et al., 2017), resulting in the transition from a relatively shallow and deeper water setting represented by the sandstone and conglomeratic deposits, to a relatively deeper quiet water environment, characterized by the finely laminated NFIF facies (Trower and Lowe, 2016).

Ernest Chi Fru 22/2/2018 09:33

**Deleted:** Sedimentary structures and microbial mat fabrics (Kiliass et al., 2011) in lithostratigraphic unit A are interpreted to record a variation between storm-dominated shallow-marine (lower shoreface), stable shallow-marine environment with low sedimentation rate in an upper to middle shoreface, and tide-influenced environments (e.g. Noffke et al., 2003; Ramos et al. 2006; Kiliass, 2011; Ossa et al., 2016).

Ernest Chi Fru 22/2/2018 09:36

**Deleted:** s 8 &

Ernest Chi Fru 23/2/2018 20:46

**Deleted:** (Stiegler et al., 2011; Trower and Lowe, 2016)

Ernest Chi Fru 23/2/2018 21:36

**Deleted:** (Lowe, 1999)

Ernest Chi Fru 23/2/2018 21:36

**Deleted:** Koike et al., 2013;

Ernest Chi Fru 22/2/2018 09:39

**Deleted:** (Trower and Lowe, 2016)

Ernest Chi Fru 22/2/2018 09:41

**Deleted:** primary granular iron formations (GIF); i.e., a facies transition from BIF-style to GIF-style IF (e.g., Bekker et al., 2010), or



### 3.3 Geochemistry

#### 3.3.1 Geochemistry of the individual Fe-rich and Si-rich bands

The SEM-EDS-electron micrographs of the NFIF thin sections reveal distinct Fe bands and Si-rich layers alternating periodically with each other in a fine sediment matrix as shown by the grain size (Figs 9 & 11 & Supplementary Figs 9-11). Laser ablation ICP-MS line analysis indicates Si and Fe count intensities in the Milos BIF-type rocks are comparable to the 2.5 Ga Precambrian BIF reference from the Kuruman IF formation, Transvaal Supergroup, South Africa (Fig. 11). The laser ablation ICP-MS data further show an inverse correlation between Fe and Si, the two major elemental components of BIFs, irrespective of the thousands of millions of years gap separating the Precambrian deposit from the recently formed Milos IF formation.

#### 3.3.2 Mineralogy of the individual Fe-rich and Si-rich bands

No other Fe(III)(oxyhydr)oxide minerals have been identified in the Cape Vani Fe-rich facies different from hematite. Electron imaging of the NFIF Fe-rich bands suggests Si, Al and K-rich phases are mostly associated with the volcanoclastic material predominated by K-feldspar clasts (Fig. 9; Supplementary Figs 10 & 11). A unique feature of the NFIF is that the hematite in the Fe-rich bands occurs in tight association with a carbonaceous material (Fig. 10C), but not for the hematite in the Fe-rich sandstones and in the MFIF. This is also the case for the CIF overlying the MFIF. Hematite showing a fluffy texture and at times presenting as framboidal particles, is sprinkled in the Si-rich cement containing traces of Al and K in the MFIF rocks (Fig. 3). Lack of association of the framboidal-iron-rich particles with S, following SEM-EDS analysis, rules out a pyrite affiliation and is consistent with the

Ernest C 27/2/2018 18:49

**Deleted:** that dramatic fluctuations in Fe concentrations control the Si to Fe ratio in both types of rocks, despite the thousands of millions of years gap between them.

non-sulfidic depositional model suggested by the sequential iron extraction redox proxy (Fig. 13D). TEM analysis suggests platy nano-Fe oxide-rich particles predominate in the NFIF and MFIF, confirmed by overlaid X-ray Energy Dispersive spectra taken from selected areas (Fig. 12) and consistent with the XRD data showing hematite in both samples. The platy hematite needles in the Milos BIF-type rocks are morphologically, and by size, comparable to hematite needles reported in the ~2.5 Ga Kuruman BIFs (Sun et al., 2015).

Unlike the Fe-rich bands, volcanoclasts in the Si-rich bands are much smaller in size, occurring mainly as fine-grained (Supplementary Fig. 8-11), signifying predominant precipitation during periods of weakened hydrothermal activity. The SiO<sub>2</sub> matrix in both the MFIF and NFIF are fine-grained, occurring mainly as amorphous opal in the NFIF (Figs 10B & 12A-B), whereas in the MFIF it is mainly present as crystalline quartz (Fig. 12C-D). Relative concentrations of Al, K and Ti in the samples are generally low, with bulk-measured concentrations in both the Si-/Fe-rich bands, together with the SiO<sub>2</sub> and Fe<sub>2</sub>O<sub>3</sub> content, strongly covarying with continental crust concentrations (Fig. 13A). Mn impregnation of the MFIF, preserved in the form of replacement layers mostly identified as cryptomelane [K(Mn<sup>4+</sup>,Mn<sup>2+</sup>)<sub>8</sub>O<sub>16</sub>] (Table 1), is below detection in the NFIF. Rare hausmannite (Mn<sup>2+</sup>Mn<sup>3+</sup><sub>2</sub>O<sub>4</sub>) was detected in a few cases in the MFIF (Fig. 10D).

### 3.3.3 Hydrothermal versus continental weathering

Trends of major elements from which CIA indices were calculated (Fig. 13B), covary with those of the continental crust (Fig. 13A). Continental crust averages, refer to the zone from the upper continental crust to the boundary with the mantle (Rudnick & Gao, 2003). The calculated CIA indices average 52 with one outlier at 22 (Fig. 13B).

No distinct relationship could be established between the CIA indices and the respective IFs or between the distinct alternating Si- and Fe-rich bands (Fig. 13). Highly weathered clay minerals resulting from the chemical decomposition of volcanic rocks, e.g., kaolinite representing maximum CIA values of 100 or 75-90 for illite, are absent in the analyzed materials. The absence of carbonates in the rocks strengthened the CIA indices, since CIA indices are expected to be lower when Ca carbonates are present (Bahlburg and Dobrzinski, 2011).  $\text{TiO}_2$  content, a detrital proxy, is mostly constant and covaries with the CIA values (Fig. 13B), suggesting little variability and limited continental weathering input. A fairly strong negative linear correlation was found between  $\text{SiO}_2$  and  $\text{Fe}_2\text{O}_3$  values normalized to  $\text{TiO}_2$  (inset, Fig. 13B).

615

#### 3.3.4 Redox reconstruction

Redox reconstruction by sequential iron extraction (Poulton and Canfield, 2005, 2011; Guilbaud et al., 2015; Sperling et al., 2015) is consistent with deposition of both the MFIF and NFIF facies beneath an anoxic, ferruginous bottom water body (Fig. 13C-D). The shale-normalized REE values ( $\text{REE}_{(\text{SN})}$ ) for both the MFIF and NFIF are consistent with previous reports (Chi Fru et al., 2013, 2015), showing patterns typical of marine sedimentary environments affected by hydrothermal activity throughout Earth's history (e.g., Planavsky et al., 2010). There is a notable absence of significant negative  $\text{Ce}_{(\text{SN})}$  anomalies for both the MFIF and NFIF (Fig. 14A-B). These observations are statistically corroborated by true Ce anomalies. Further, the  $\text{Eu}/\text{Eu}^*$  anomaly averages for the MFIF and NFIF and the distinct Fe-/Si-rich bands, suggest a  $\sim 2\times$  higher  $\text{Eu}/\text{Eu}^*$  signal for the Si-rich bands relative to the Fe-rich bands and between the MFIF and NFIF deposits (Fig. 14C). Average Pr and

Ernest C 27/2/2018 21:13

**Deleted:** calculated as  $\text{Ce}/\text{Ce}^*$  ( $\text{Ce}_{(\text{SN})}/0.5\text{Pr}_{(\text{SN})} + 0.5\text{La}_{(\text{SN})}$ ) and  $\text{Pr}/\text{Pr}^*$  ( $\text{Pr}_{(\text{SN})}/0.5\text{Ce}_{(\text{SN})} + 0.5\text{Nd}_{(\text{SN})}$ ) and considered significant when  $\text{Ce}/\text{Ce}^*$  and  $\text{Pr}/\text{Pr}^*$  is less than and greater than 1, respectively (Bau et al., 1996; Planavsky et al., 2010) (Fig. 14B).

635 | Yb shale-normalized ratios (Pr/Yb\*), a light vs. heavy REE enrichment proxy  
636 | (Planavsky et al., 2010), indicate similar depleted levels of light and heavy REE in  
637 | both the NFIF and MFIF, as well as in the Fe- and Si-rich bands (Fig. 14C). This  
638 | independent verification of the anoxic depositional conditions using the sequential Fe  
639 | proxy, suggests the NASC normalization protocol effectively captures the redox  
640 | depositional conditions of the Milos IF.

641

#### 642 3.4 Lipid biomarker distribution and chemotaxonomy

643 | Bulk  $\delta^{13}\text{C}_{\text{org}}$  averaged  $-25.4\text{‰}$  (SD: $\pm 0.22$ );  $-25.2\text{‰}$  ( $\pm 0.26$ ) for NFIF Fe-/Si-rich  
644 | bands and  $-25.6\text{‰}$  (SD: $\pm 0.12$ ) for bulk MFIF, respectively (Table 2). A fractionation  
645 | effect between the alternating Fe-/Si-rich layers ( $\Delta^{13}\text{C}_{\text{Fe-rich NFIF-Si-rich NFIF}}$ ) is estimated  
646 | to be  $\sim 0.23\text{‰}$  (SD: $\pm 0.036$ ), while  $\Delta^{13}\text{C}_{\text{Fe-rich NFIF-MFIF}}$  and  $\Delta^{13}\text{C}_{\text{Si-rich NFIF-bulk MFIF}}$  is  
647 |  $0.13\text{‰}$  (SD: $\pm 0.11$ ) and  $0.36\text{‰}$  (SD: $\pm 0.14$ ), respectively. These differences are small  
648 | and within the margin of error of analysis, suggesting no strong distinction in  $\delta^{13}\text{C}_{\text{org}}$   
649 | preserved in the different IFs and their various facies. They are interpreted to mean  
650 | similar carbon fixation processes operated during intervals of predominant Si and  
651 | Fe(III)(oxyhydr)oxides deposition in both IFs. Attempts to discriminate between these  
652 | environments by lipid biomarker analysis revealed mainly  $\text{C}_{16}\text{-C}_{19}$  fatty acid methyl  
653 | esters (FAME) in the Fe-rich NFIF bands and in bulk MFIF, while the Si-rich NFIF  
654 | bands contain mainly  $\text{C}_{12}\text{-C}_{21}$  FAMEs, suggesting either selective preservation (lipid  
655 | recovery was lower in the Fe-rich MFIF bands) or shifts to different potential  
656 | biological populations during the deposition of the different layers. Preserved lipids  
657 | discriminate against typical microbial lipid biomarkers like hopanoids, while  $\text{C}_3$  plant  
658 | FAME are detected in all studied materials (Fig. 15). However, the anaerobic bacteria  
659 | indicator,  $10\text{MeC}_{16:0}$  FAME, was identified in a few bands.

660

## 661 **4 Discussion**

### 662 **4.1 Sedimentological processes**

663 The three sub-basin division of the CVSB is consistent with previous proposals  
664 suggesting that sedimentation within the CVSB was characterized by active  
665 synvolcanic rifting which must have been important in shaping basin topography and  
666 the creation of sub-basin architecture (Papanikolaou et al., 1990; Stewart and McPhie,  
667 2006; Liakopoulos et al., 2001; Papavassiliou et al., 2017). Moreover, this tectonic  
668 regime would suggest that the location(s) of volcanism were continually changing  
669 relative to the two stratigraphic sections, which themselves were also being affected,  
670 i.e. changes in depositional water depth and sedimentation style or and/or that local  
671 submarine or subaerial topographic highs impeded the lateral continuity of  
672 sedimentary units (Stewart and McPhie, 2006). Chi Fru et al. (2015) have suggested  
673 there is an upward deepening of the overall depositional setting recorded in the “Little  
674 Vani” section, consistent with rifting during CVSB infilling time.

675 The CVSB floored by dacitic/andesitic lava domes and overlain by  
676 volcanoclastic infill, dates back to Upper Pliocene-Lower Pleistocene. A complex  
677 mosaic of lithologically diverse sedimentary units (blocks), confined by neotectonic  
678 marginal faults, characterizes the CVSB (Fig. 2). The most pronounced of these faults  
679 being the NW-trending Vromolimni-Kondaros fault (Papanikolaou et al., 1990) that  
680 has been proposed as the trigger of the hydrothermal activity that deposited Mn ore in  
681 the CVSB (Papanikolaou et al., 1990; Liakopoulos et al., 2001; Alfieris et al., 2013;  
682 Papavassiliou et al., 2017). The stratigraphically tight coupling between Mn and Fe  
683 deposition, linked by Fe oxide minerals in feeder-veins, and positive Eu anomalies  
684 (Fig. 14) indicating vent-sourced Fe (Maynard, 2010), associate Fe mineralization to

685 fault-triggered hydrothermalism in the CVSB. This is consistent with models of  
686 geothermal fluid circulation along fault lines as conduits for the Mn-rich fluids that  
687 formed the Milos Mn ore deposit (Hein et al., 2000; Liakopoulos et al., 2001; Glasby  
688 et al., 2005; Kiliyas, 2011; Papavassiliou et al., 2017). More importantly, the overall  
689 complex neotectonic structure of the CVSB (Papanikolaou et al., 1990) would explain  
690 the creation of restricted basins, with sedimentological, lithological and geothermal  
691 conditions that enabled the development of unique biogeochemical circumstances in  
692 which the NFIF and MFIF formed.

693 The presence of the three depositional basins is supported by the fact that the  
694 sequence lithologies in each fault-bound unit are characterized exclusively by  
695 occurrences of specific and variably thick stratigraphic packages that tend to be  
696 absent in others. For example, the MFIF occurs restricted to basin 1 and the NFIF to  
697 Basin 3. Basin 2 is further distinguished by 35-50 m thick interbedded ore-grade Mn-  
698 mineralized and glauconitic sandstones/sandy tuffs, much less developed in Basins 1  
699 and 3 (Fig. 2). The presence or absence of a stratigraphic sequence, together with its  
700 thickness variation, are interpreted as a result of local syntectonic sediment formation  
701 conditions in each basin as a result of block tectonic movements along fault lines  
702 (Papanikolaou et al., 1990). It may also be attributed to unique basin scale water  
703 column redox conditions (e.g. Bekker et al., 2010, and references therein), post-  
704 depositional erosion and changing sea level stand (Cattaneo & Steel, 2000).

705 The lack of hydrothermal feeder veins or seafloor exhalative structures (i.e.,  
706 chimneys) in the MFIF and NFIF lithologies, suggests that hydrothermal Fe(II) was  
707 delivered by diffuse flow and that the Milos-IF formed on the seafloor.  
708 Further, mineralisation of the MFIF is suggested to have occurred during two major  
709 hydrothermal venting stages. The first produced the MFIF and the second

contaminated it with cryptomelane. Cryptomelane in the MFIF is therefore not a replacement product of primary Mn oxides formed during the deposition of the MFIF, because the anoxia prevailing in Basin 1 at the time (Figs 2 & 13C) would have precluded the precipitation of Mn oxide minerals, hinting that a second phase hydrothermal fluid emission rich in dissolved Mn, directly precipitated cryptomelane from solution as a secondary mineral relative to the primary Fe(III)(oxyhydr)oxides in the MFIF. This occurred during an episode when the MFIF deposit must have been exposed to oxygenated fluids, most likely through mixing with seawater at depth, indicated by the abundance of cryptomelane at the base of the MFIF. Our model for cryptomelane precipitation in the MFIF is therefore different from the one suggesting diagenetic transformation of primary Mn ores at Milos (Hein et al., 2001; Liakopoulos et al., 2001; Papavassiliou et al. 2017).

Geomorphological/chemical reconfiguration orchestrated the deposition of the NFIF in a deeper, small-restricted basin (Fig. 2). The deepening of Basin 3 is reflected in the underlying graded conglomerate bed that exhibits an upward fining trend, followed by transition into the fine-grain NFIF. The conglomerate bed may represent rapid deposition during a high-energy event, i.e. storm or mass flow, whereas the upward fining in the bed is better explained by the depositional mechanism losing energy through time. These high-energy conditions apparently must have ceased during the deposition of the overlying NFIF, where we interpret that increased abundance of finely laminated IF and decreased evidence of storm and/or mass flow reworking reflects deepening conditions. The hypothesized deepening of Basin 3 is consistent with the interpretation that active rifting was an important mechanism in the formation of the CVSB (Papanikolaou et al., 1990).

Ernest Chi Fru 22/2/2018 09:53

**Deleted:** The deepening of Basin 3 is strongly demonstrated by an underlying fine upward grading of a transgressive-type Fe-rich lag deposit, that transitions into the NFIF. This uplifting into shallower water event that prompted second generation deposition of Mn oxides in Basin 2 and the substitution of Fe(III)(oxyhydr)oxides by Mn in sub-Basin 1, potentially triggered this environmental change in Basin 3. The MFIF and NFIF sequences are therefore temporally and spatially distinct (Fig. 2).



## 4.2 Formation Mechanism of The Milos BIFs

### 4.2.1 Paragenetic sequence

It is stressed that the previously generalized model proposed for biological deposition of the Milos IF, refers exclusively to parts of what is now designated as MFIF (Chi Fru et al., 2013). The NFIF is strongly banded, but does not display the typical microfossils seen in the MFIF, where diffused microbanding apparently relates to the distribution of microbial mats in thin sections (Chi Fru et al., 2013, 2015). The distinction of microcrystalline quartz and amorphous silica phases in the MFIF and NFIF, respectively, together with nano-crystalline hematite particles, suggests a primary amorphous silica origin in both deposits, diagenetically transformed to quartz in the MFIF. The difference in silica crystallinity between the IFs is concurrent with the older age predicted for the MFIF relative to the NFIF, from reconstructed sequence stratigraphy (Fig. 2). Hematite in BIFs is generally interpreted, based on thermodynamic stability, to be a transformation of various primary Fe(III) minerals, with ferrihydrite often proposed as the principal precipitate from the water column (Glasby and Schulz, 1999; Bekker et al., 2010; Johnson et al., 2008; Percoits et al., 2009). It is thought that acidic pH yields mainly goethite while hematite is produced at circumneutral pH (Schwertmann and Murad, 2007). The notable absence of diagenetic magnetite and Fe carbonates (siderite and ankerite), point to negligible coupling of primary Fe(III) oxyhydroxides reduction to organic matter oxidation by the dissimilatory iron-reducing bacteria during burial diagenesis (Johnson et al., 2008). Minor occurrence of iron-silicate phases (Chi Fru et al., 2015) indicates an origin of the hematite precursor in seawater independent of the iron silicate proposed in some cases (Fischer and Knoll, 2009; Rasmussen et al., 2013, 2014). The up to 50 wt% Fe content recorded in the Fe-rich bands, indicate that large amounts of

772 dissolved Fe(II) was intermittently sourced and deposited as primary Fe(III) minerals,  
773 through various oxidative processes in the depositional basin.

774 Importantly, the CIA analysis does not support mass weathering and  
775 mineralization of terrestrial Fe and Si, in agreement with the absence of rivers  
776 draining into the CVSB (Chi Fru et al., 2013). The specific identification of plant  
777 biolipids would at face value imply post-depositional contamination. However,  
778 samples were sawn to remove exposed layers and only the laminated bands for the  
779 NFIF were analyzed. Modern sediments from Spathi bay, located Southeast of Milos  
780 Island where hydrothermal activity is presently ensuing at 12.5 m below sea level,  
781 revealed similar plant lipids as recorded in the Quaternary IF (Fig. 15G). Post-  
782 depositional contamination with terrestrial plant lipids is therefore ruled out for the  
783 idea that recalcitrant plant biomass probably entered the sediments via seawater  
784 entrainment at the time of deposition (see Naden et al., 2005). This finding  
785 necessitates the careful interpretation of bulk  $\delta^{13}\text{C}_{\text{org}}$  values obtained from both the  
786 modern and ancient Milos sediments, involving in situ and ex situ biological  
787 contributions to  $^{13}\text{C}_{\text{org}}$  fractionation by various known carbon fixation pathways  
788 (Preuß et al., 1989; Berg et al., 2010).

#### 789 **4.2.2 Tectono-sedimentary processes and band formation**

791 Fluctuation in hydrothermal activity is proposed to account for the banding in the  
792 NFIF (Fig. 16), under redox depositional conditions inferred to be mainly reducing  
793 for both investigated IFs, consistent with previous reports (Chi Fru et al., 2013, 2015).  
794 Positive Eu anomalies indicate a hydrothermal origin for all but one of the sample  
795 suite (Fig. 14A). However, statistically calculated  $\text{Eu}/\text{Eu}^*$  anomalies ( $\text{Eu}_{(SN)}/$   
796  $(0.66\text{Sm}_{(SN)} + 0.33\text{Tb}_{(SN)})$ ) to correct for differences in Gd anomalies commonly

Ernest C 26/2/2018 22:26

**Deleted:** Such indication of mixing of the hydrothermal fluids with seawater may be interpreted to negate a reducing depositional environment as suggested by the Ce anomalies. However, Pichler & Veizer (1999) demonstrated that in the unconfined seafloor shallow hydrothermal vent fields at Tatum Bay, Papua New Guinea, experiencing little or no water column stratification, as low as 11% seawater is involved in the precipitation of Fe(III)(oxyhydr)oxides from hydrothermal fluids and at maximum 57%. It is therefore suggested that seawater mixing during deposition was at the lower limits. This is demonstrated by the REE analysis and the presence of anaerobic bacteria biomarkers in the NFIF formation, coupled to sediment lithology and stratigraphy, as explained below.

815 encountered in seawater (Planavsky et al., 2010) are in the range of 0.1-0.58,  
816 averaging 0.42. The lack of statistically significant true negative Ce anomalies (Fig.  
817 14B) supported by sequential Fe redox reconstruction (Fig. 3C-D; Planavsky et al.,  
818 2010; Poulton and Canfield, 2005, 2011; Guilbaud et al., 2015; Sperling et al. 2015).  
819 indicate a reducing depositional environment for both The MFIF and the NFIF.

820 CIA analyses traditionally provide relative information on contributions from  
821 chemical weathering to sediment deposition, linked to operative hydrological and  
822 climatological patterns on land. This information is often gleaned from ancient and  
823 modern soils and from reworked siliclastic deposits in marine basins (Maynard, 1993;  
824 Bahlburg & Dobrzinski, 2011). The calculated CIA values, however, are closer to the  
825 range obtained for unweathered and or only minimally weathered volcanic rocks (e.g.,  
826 Nesbitt & Young, 1982; Bahlburg & Dobrzinski, 2011), thus pointing to a  
827 predominantly volcanic and/or hydrothermal provenance for the clastic sedimentary  
828 materials in the IFs.

829 It has been suggested that the release of reduced submarine hydrothermal fluids  
830 contributed towards maintaining water column anoxia during the deposition of  
831 Precambrian BIFs (Bekker et al., 2010). The calculated Eu anomalies (Fig. 14) and  
832 petrographic data showing volcanoclastic detritus (i.e., K-feldspar, sanidine, tridymite,  
833 cristobalite) as key rock components are in agreement with a submarine hydrothermal  
834 source for the investigated IFs. The coarse volcanoclastic detritus embedded in the Fe-  
835 rich bands compared to the finer particles in the Si-rich layers, highlights rapid  
836 oxidation of Fe(II) that coincided with periodic cycles of hydrothermal/volcanic  
837 discharge of new materials into the water column. However, the fine-grained nature  
838 of both the MFIF and NFIF deposits suggests that deposition likely occurred away  
839 from where such activity was occurring or that volcanic/hydrothermal discharge of Fe

Ernest C 23/2/2018 13:26

**Deleted:** The values are closer to the anoxic water column values calculated for Archean IFs, compared to Paleoproterozoic IFs (Planavsky et al., 2010), which may be due to their deposition in an active volcanic center like most of the Archean Agglomeration BIFs (Bekker et al., 2010; Chi Fru et al., 2015).

Ernest C 23/2/2018 15:24

**Deleted:** These reducing conditions are confirmed and shown to have been mainly ferruginous by sequential iron reconstruction of depositional setting redox. The sequential iron proxy records the immediate redox state of the water mass beneath which the sediment accumulated ().

Ernest C 27/2/2018 19:04

**Deleted:** indices traditionally provide

Ernest C 27/2/2018 19:05

**Deleted:** indices

and Si was non-eruptive and disruptive. The Fe-rich bands repetitively revealed hematite grains cementing the denser volcanoclastic fragments that gradually diminish upwards into a zone of fine-grained hematite before transitioning into Si-rich bands consisting mainly of finer volcanoclastic detritus. These observations provide three valuable interpretational considerations for proposing a model for the formation of the alternating Si and Fe-rich bands.

1. The Si and Fe oxides-rich bands are primary precipitates formed in the water column, by a process in which the precipitation of amorphous Si occurred during quiescent non-volcanic intervals, with the oxidation and precipitation of reduced Fe intermittently introduced into the water column by volcanic/hydrothermal activity to form the Fe oxides.
2. The repetitive zonation of distinct particle sizes, suggests density gradient sedimentation that requires a water column-like environment, rather than diagenetic alteration of pre-formed sediments by hydrothermal fluids.
3. The reducing depositional conditions do not support sediment diagenesis as an alternative model for explaining the origin of the Milos IF. This is because the oxidation of ferrous Fe supplied in reduced hydrothermal fluids, must interact with a sizeable pool of oxygen, enabling microaerophilic bacteria oxidation of ferrous iron to Fe(III)(oxyhydr)oxides (Johnson et al., 2008). Otherwise, light-controlled photoferrotrophy, an extremely rare sediment characteristic, precipitates Fe oxides in the absence of oxygen in sunlight environments (Weber et al., 2006).

#### 4.2.3 Biological involvement

Ernest C 26/2/2018 21:51

**Deleted:** <#>The style of deposition of the MFIF and NFIF is distinct from the post-depositional infilling of a porous sandstone sediment matrix during the formation of the Mn ores. Instead the deposition of the MFIF and NFIF in restricted portions in the basins not associated with previously accumulated sandstones, and the difficulty and lack of evidence to provide a viable biogeochemical mechanism for the formation of the even bands of alternating Si and Fe-rich layers of several meters high and wide, does not support post-depositional pore filling of a porous sandstone matrix by Fe, as a potential pathway to the formation of the Milos IF. .

897 Hematite precipitation in the MFIF on microbial filaments (Chi Fru et al., 2013) was  
 898 previously used to propose a generalized basin-scale mechanism for the deposition of  
 899 Fe-rich rocks in Cape Vani. However, such filaments are absent in the NFIF, while  
 900 pure hematite grains are tightly bound to relics of an organic matter signal carrying a  
 901 maximum  $\delta^{13}\text{C}_{\text{org}}$  signature of -25‰ (Table 2). Similar processes are recorded in  
 902 modern marine sediments where interactions between Fe and free organic matter has  
 903 been reported to enable the preservation up to 21.5wt% of total organic carbon over  
 904 geological time scales (Lalonde et al., 2012). Moreover, Fe generally traps and  
 905 preserves organic matter at redox interfaces (Riedel et al., 2013). The data appear to  
 906 suggest that the mechanism of Fe(III) (oxyhydr)oxide precipitation and preservation  
 907 varied between the two IFs. The photoferrotrophic-like filamentous fossils reported in  
 908 the MFIF (Chi Fru et al., 2013), are absent in the NFIF. This does not, however, rule  
 909 out the potential role of microbial involvement in Fe(II) oxidation, as diverse  
 910 microbial taxa carry out this process, several of which are non-filamentous (Chi Fru et  
 911 al., 2012). However, our data is insufficient to enable clear quantification of the levels  
 912 of abiotic vs. biotic contribution to Fe(II) oxidation in the NFIF. Nevertheless, the  
 913 inferred predominantly anoxic depositional conditions as explained above, together  
 914 with the identification of anaerobic bacteria biomarkers in the laminated bands,  
 915 intuitively favor significant contribution of anaerobic biological Fe(II) oxidation in  
 916 the precipitation of primary Fe(III)(oxyhydr)oxides in the NFIF. See Weber et al.,  
 917 2006, for a review of potential biological pathways to anaerobic Fe(II) oxidation.

918 Briefly, anaerobic microbial Fe(II) oxidation can proceed via nitrate reduction  
 919 and by photoferrotrophy to deposit Fe(III)(oxyhydr)oxides. These mechanisms have  
 920 been linked to microbial contribution to BIF formation (Weber et al., 2006; Kappler et  
 921 al., 2005) and also for the MFIF (Chi Fru et al., 2013). However, it is also possible

Ernest C 27/2/2018 19:08

**Deleted:** lack of similar

Ernest C 27/2/2018 19:08

**Deleted:** ,

Ernest C 27/2/2018 19:09

**Deleted:** since

925 that microaerophilic neutrophilic Fe(II)-oxidizing bacteria likely played an important  
926 role, assuming a depositional setting analogous to the Santorini caldera and Kolumbo  
927 shallow submarine volcanoes, where such low-O<sub>2</sub>-dependent microbial Fe(II)  
928 oxidation has been identified to actively precipitate Fe(III) (oxyhydr)oxides (Kiliass et  
929 al., 2013b; Camilli et al., 2015). It appears that in the MFIF, precipitating  
930 Fe(III)(oxyhydr)oxide minerals were bound and preserved free of organic carbon or  
931 that such organic carbon was diagenetically degraded. As was previously shown,  
932 Fe(III)(oxyhydr)oxides completely replaced the organic content of the filamentous  
933 microfossils in the MFIF (Chi Fru et al., 2013).

934 The 10MeC<sub>16:0</sub> FAME identified in the rocks has been reported in anaerobic  
935 organisms coupling nitrite reduction to methane oxidation (Kool et al., 2012), in  
936 sulfate and iron-reducing bacterial species such as *Desulfobacter*, *Desulfobacula*  
937 (*Bühning* et al., 2005; Dowling et al., 1986; Taylor and Parkes, 1983), *Geobacter*,  
938 *Marinobacter* and the marine denitrifier, *Pseudomonas nautical* (Kool et al., 2006;  
939 *Bühning* et al., 2005; Dowling et al., 1986). It had previously been proposed that post-  
940 depositional denitrification was a potential pathway for early organic matter removal,  
941 justified by the low rock organic carbon and nitrogen content in the Milos BIF-type  
942 rocks (Chi Fru et al., 2013, 2015; Table 2). Equally, the detected 10MeC<sub>16:0</sub> FAME  
943 has also been found in anaerobic oxidation of methane (AOM) communities (Alain et  
944 al., 2006; Blumenberg et al., 2004), originating from sulfate reducing bacteria.  
945 However, bulk sediment  $\delta^{13}\text{C}_{\text{org}}$  of  $-20\text{‰}$  does not reflect AOM activity that is  
946 expected to produce bulk  $\delta^{13}\text{C}_{\text{org}}$  values that are  $\leq -30\text{‰}$ . Low 10MeC<sub>16:0</sub> FAME  
947 concentrations frustrated attempts at acquiring its compound specific isotopic  
948 signature to enable further biomolecular level reconstruction of active microbial  
949 metabolisms to explain Fe deposition mechanisms.

It is nevertheless puzzling why potential microbial biomarkers typical of marine or hydrothermal vent environments are hardly preserved in the rocks, given that microfossil evidence indicates a vast community of diverse prokaryotic assemblages in the adjacent MFIF (Chi Fru et al., 2013, 2015). Moreover, sediments of the modern Milos hydrothermal system and elsewhere on the HVA, are ubiquitously colonized by microbial life, characterized by the marked large-scale absence or low abundance of higher life forms, including plants (Kiliass et al., 2013b; Camilli et al., 2015; Oulas et al., 2015). One possibility could be the discriminatory preservation of lipids related to their selectivity and reactivity towards Fe(III)(oxyhydr)oxides and clays or different pathways to diagenetic degradation (e.g., Canuel & Martens, 1996; Lü et al., 2010; Riedel et al., 2013). As noted, the carbonaceous materials in the BIF-type NFIF rocks occur in tight association with hematite.

Importantly, prokaryotic biomarkers are suggested to poorly preserve in these young BIF analogues. This raises the possibility that this may provide an important explanation for why lipid biomarkers are yet to be extracted from Precambrian BIFs. Moreover, the data are compatible with the low  $C_{org}$  recorded in BIFs of all ages, suggesting that the low  $C_{org}$  abundance may not be due to metamorphism as often proposed (Bekker et al., 2010) or to  $C_{org}$  oxidation by dissimilatory iron reducing bacteria to form  $^{13}C$ -depleted siderite and ankerite during diagenesis (Johnson et al., 2008; Bekker et al., 2010). The Milos BIF-type rocks are unmetamorphosed and lack iron carbonate, yet have vanishingly low  $C_{org}$  levels similar to the ancient metamorphosed BIFs. However, an alternative possibility is that the iron oxides may have been reduced through biological oxidation of organic carbon, but carbonate saturation was not reached (Smith et al., 2013).

975

#### 976 4.2.4 Mn layers and the deposition of the Si-Fe-rich facies

977 [Cryptomelane \[K\(Mn<sup>4+</sup>,Mn<sup>2+</sup>\)<sub>8</sub>O<sub>16</sub>\]](#), which commonly occurs in oxidized Mn  
978 [deposits resulting from mineral replacement and as open space fillings \(Papavassiliou](#)  
979 [et al., 2016\)](#), is also common in the MFIF. This supports the idea of post-depositional  
980 [impregnation of the base of the MFIF by Mn-rich fluids](#). Microscopic analysis  
981 supports the epigenetic origin of the Mn in the MFIF by revealing Mn oxides growing  
982 along fractures, impregnating and replacing Fe minerals (Fig. 4B-F). The  
983 macroscopically evident thinning out to disappearance of such Mn-rich horizons up  
984 the MFIF, coupled by their development along microfractures emphasizes this  
985 epigenetic origin. Mn is not a common feature of the NFIF, even though it sits on top  
986 of a thin sandstone layer that is highly [mineralized with](#) Mn, locally forming the cap  
987 of the main Mn ore at Cape Vani. The generally accepted view is that Mn-rich  
988 hydrothermal fluids rose and mineralized the Cape Vani sandstones (Hein et al., 2000;  
989 Liakopoulos et al., 2001; Glasby et al., 2005). Based on the stratigraphic location of  
990 the MFIF, which pre-dates the Mn-rich sandstones, it is proposed that impregnation of  
991 the MFIF by Mn was coeval with large-scale Mn ore mineralization of the Cape Vani  
992 sandstones, implying the entire basin was likely oxygenated at the time. The lack of  
993 Ce anomalies, [confirmed by the sequential Fe extraction proxy data](#), suggests that  
994 both the MFIF and the NFIF formed in anoxic settings. Similar data for the Mn oxides  
995 have suggested formation in oxic settings (Glasby et al., 2005; Chi Fru et al., 2015).  
996 [This implies that Mn epigenetically replaced the MFIF](#), either because the basin was  
997 tectonically uplifted into a high-energy oxygenated shallow water setting or that sea  
998 level dropped, leading to partial metasomatism of the base of MFIF, when oxygenated  
999 seawater mixed with [reduced](#) hydrothermal fluids and precipitated Mn. The lack of

Ernest C 27/2/2018 19:11

**Deleted:** Cryptomelane [K(Mn<sup>4+</sup>,Mn<sup>2+</sup>)<sub>8</sub>O<sub>16</sub>], commonly occurring in oxidized manganese deposits resulting from mineral replacements and as open space fillings (Papavassiliou et al., 2016), common in MFIF, supports the idea of post-depositional impregnation of the base of the MFIF by Mn-rich fluids as discussed above.

Ernest C 27/2/2018 19:13

**Deleted:** However, more sensitive proxies are needed to resolve and confirm the stratigraphic and REEs-dependent interpretation of potential redox conditions.



1012 significant Ce anomalies in the dataset, combined with the inferred deepening of basin  
1013 3 and the anoxic depositional conditions suggested by the sequential iron redox proxy,  
1014 further indicate that for the final deposition of the NFIF, an eventual deepening event  
1015 must have been triggered, resulting in deoxygenation of parts of the CVSB.

1016 All of this is feasible with the three-basin-fault-bounded hypothesis as a  
1017 requirement for movement along fault lines in response to temporal tectonic  
1018 activation. The upward sequence transition from the Mn-rich sandstone facies,  
1019 through the pebbly conglomerate and the final termination in the overlying mud-  
1020 grained NFIF (Fig. 8B), reflect sedimentary features formed during multiple changes  
1021 in seawater levels (Cattaneo & Steel, 2000).

1022 Uplifting is suggested by potential weathering of the NFIF to form the  
1023 ferruginous duricrust cap. Comparable ferruginous layers on Precambrian BIFs are  
1024 linked to pervasive subaerial chemical weathering, via the dissolution of the silica-  
1025 rich layers and precipitation of relatively stable Fe oxides in the spaces between more  
1026 resistant hematite crystals (e.g., Dorr, 1964; Shuster et al., 2012; Levett et al., 2016).  
1027 This collective evidence supports the existence of a geodynamic tectonic system  
1028 capable of producing shallow oxic to deeper anoxic basin conditions at different times  
1029 that would explain the existence of Mn and Fe oxide layers within the same  
1030 sedimentary sequence. For example, it is common knowledge that both Fe and Mn  
1031 oxides will precipitate in the presence of oxygen (Roy, 1997, 2006), with kinetic rates  
1032 usually being faster for the oxidation of reduced Fe than reduced Mn. In the Fe(II)-  
1033 rich conditions that prevail in anoxic settings, abiotic reactions between Fe(II) and Mn  
1034 oxides, produce Fe(III) leading to the dissolution of the Mn oxides to form reduced  
1035 Mn, implying Mn oxides should not accumulate (Dieke, 1985). Moreover, under these  
1036 conditions, biological precipitation of Fe(III) can occur rapidly, leaving dissolved Mn

Ernest Chi Fru 11/3/2018 22:22

**Deleted:** strongly implies that the underlying Mn-rich facies and NFIF layers formed in shallower and deeper waters, respectively, or that they are separated by an erosional unconformity underlying Mn-rich layer into the conglomeratic deposit

Ernest Chi Fru 11/3/2018 22:38

**Deleted:** This study proposes that the NFIF that overlies the transgressive-type conglomeratic lag along an erosional contact surface was likely deposited during maximum flooding, when the basin became stagnant and stratified, and subsequently was uplifted to emergence

Ernest C 23/2/2018 13:31

**Deleted:** Similar transgression-type lithologies are indicated to have regulated primary sedimentation styles during the deposition of nearshore Paleoproterozoic BIFs (Pufahl and Fralick, 2004; Pufahl et al., 2014).

Ernest Chi Fru 23/2/2018 12:29

**Deleted:** Moreover, deposition of BIFs in sandstone/grainstone-dominated environments has also been suggested for Precambrian IFs (Simonson, 1985; Simonson and Goode, 1989; Pufahl and Fralick, 2004).

Ernest C 26/2/2018 22:08

**Deleted:** the

in solution to be deposited when oxygen becomes available. Given that the hydrothermal fluids of the Hellenic Volcanic Arc are commonly enriched in both reduced Fe and Mn, the deposition of the MFIF and NFIF therefore implies there was an existing mechanism that enabled the kinetic discrimination and deposition of the oxides of Fe and Mn into separate settings, most likely dependent on prevailing redox conditions. The accumulation of the ferruginous duricrust layer, overprinted by redox sensitive Mn-nodules, above the NFIF indicates a new shallowing event might have terminated the formation of the NFIF.

#### **4.2.5 Modern analogues on the HVA**

Mechanistic explanation for the development of potential stratified waters and reducing conditions during the deposition of the Milos BIF is problematic. However, evidence is available from present shallow submarine hydrothermal analogues in the central part of the HVA, to which the CVSB belongs. These include:

(1) The crater floor of the Kolumbo shallow-submarine volcano (~600×1200 m), which rises from 504 to 18 m below sea level near Santorini, (Sigurdsson et al., 2006; Kiliass et al., 2013b).

(2) The N part of Santorini's submerged caldera walls, which rises from 390 m below sea level to over 300 m above sea level (Druitt et al., 1999; Friedrich et al., 2006; Nomikou et al., 2013; Camilli et al., 2015).

(3) The coastal embayments at the Kameni emergent volcanic islands in the centre of the Santorini caldera (Hanert, 2002; Nomikou et al., 2014; Robbins et al., 2016).

The benthic waters within Kolumbo's crater potentially sustain O<sub>2</sub> depleted conditions via stable CO<sub>2</sub>-induced water column densification, and accumulation of

1086 acidic water (pH~5), extending ~10 m above the CO<sub>2</sub> venting crater floor (Kilias et  
1087 al., 2013b). This phenomenon is believed to lead not only to obstruction of vertical  
1088 mixing of bottom acidic water, but also to O<sub>2</sub> deprivation by precluding efficient  
1089 transfer of oxygenated surface seawater into the deeper crater layer. In addition,  
1090 diffuse CO<sub>2</sub> degassing is believed to be linked to the formation of Fe microbial mats  
1091 and amorphous Fe(III) oxyhydroxides on the entire Kolumbo crater floor (Kilias et  
1092 al., 2013b). Prerequisites for the O<sub>2</sub>-depleted conditions to happen are the closed  
1093 geometry of the Kolumbo crater and the virtually pure CO<sub>2</sub> composition of the  
1094 released hydrothermal vent fluids that produce O<sub>2</sub>-stratification along a stable CO<sub>2</sub>-pH  
1095 gradient.

1096 A similar scenario is reported for the Santorini caldera, where large (~5 m  
1097 diameter) CO<sub>2</sub>-rich, acidic (pH, ~5.93) hydrothermal seafloor pools and flow  
1098 channels, develop within m-thick microbial Fe-mats on the seafloor slope at 250-230  
1099 m below sea level. Persistent hypoxia exists in these pools, representing concentrated  
1100 seafloor CO<sub>2</sub> accumulation centers generated by hydrothermal venting (Camilli et al.,  
1101 2015). Here, the dissolved O<sub>2</sub> content (~80 µM or less) in the pools is ~40 % depleted  
1102 relative to the surrounding ambient seawater (Camilli et al., 2015). These hypoxic  
1103 conditions are comparable to or even lower than those measured in the CO<sub>2</sub>-rich  
1104 oxygen minimum zones of coastal oceans, relative to seawater existing in equilibrium  
1105 with atmospheric pO<sub>2</sub> and pCO<sub>2</sub> pressures (Paulmier et al., 2008, 2011; Franco et al.,  
1106 2014). These conditions enable strong redox stratification of the pool waters, in which  
1107 unique Si- and Fe-rich microbial mats are associated with amorphous opal and  
1108 Fe(III)(oxyhydro)xides (Camilli et al., 2015). Importantly, the Fe microbial mats in  
1109 these CO<sub>2</sub>-rich hypoxic pools are affiliated with specific microaerophilic Fe(II)-  
1110 oxidizing bacteria that accumulate Fe(III) oxyhydroxides (Camilli et al., 2015; Oulas

1111 et al., 2015). These Fe bacteria are implicated in the deposition of the Precambrian  
1112 BIFs (Konhasuer et al., 2002; Planavsky et al., 2009; Bekker et al., 2010).

1113 Hypoxia is also associated with the water column of the Fe(III)-rich coastal  
1114 embayments and their hydrothermal vents ( $\leq 1.0$  m water depth), Kameni islands  
1115 (Hanert, 2002; Robbins et al., 2016 and references therein). Venting fluids are warm  
1116 (20-40 °C), acidic to circumneutral (pH 5.5-6.9), enriched in CO<sub>2</sub>, Fe and Si  
1117 (Georgalas & Liatsikas, 1936; Boström et al., 1990; Handley et al., 2010; Robbins et  
1118 al., 2016). Water column stratification is expressed as decreasing O<sub>2</sub> with depth that is  
1119 positively related to Fe(III)(oxyhydr)oxide density and microaerophilic Fe(II)-  
1120 oxidizing bacterial prevalence (Hanert, 2002). Robbins et al. (2016) found that  
1121 Fe(III)-rich suspended particulate material in these “Fe bays” may be associated with  
1122 anoxia, extending up to the air-seawater interface, near the hydrothermal vents  
1123 (Hanert, 2002). They consist of ferrihydrite, goethite and microaerophilic Fe(II)  
1124 oxidizers.

1125 | [However,](#) the biogeochemical occurrence of these phenomena within the  
1126 localized confines of the Santorini caldera and Kolumbo crater, may however be  
1127 difficult to achieve in ordinary shallow submarine hydrothermal settings, such as  
1128 those occurring on the coast of present day Milos. The same may be true for Tatum  
1129 Bay, where non-volcanic and unconfined diffuse hydrothermalism is widespread  
1130 (Dando et al., 1996; Pichler & Dix, 1996; Pichler & Veizer, 1999; Stüben et al., 1999;  
1131 Rancourt et al., 2001; Varnavas et al., 2005).

1132 In the Kolumbo and Santorini hydrothermal fields, benthic pH averages 5.5 and  
1133 the deposition of carbonates is markedly absent (Kiliyas et al., 2013b, Camilli et al.,  
1134 2015; Robins et al., 2016). This conforms to observations in the MFIF and NFIF units  
1135 where carbonate mineralization is not detected, thereby suggesting a similar low pH

depositional environment for both the MFIF and NFIF. Ubiquitous Fe(III)(oxyhydr)oxide precipitation and enriched Si content are prevalent in the CO<sub>2</sub>-rich-hypoxic shallow submarine Santorini caldera slope pools and the Kameni Fe-embayments where sulfide precipitation is inhibited (Camilli et al., 2015), or extremely rare (Robbins et al., 2016). Such sulfide-poor conditions are critical for the formation of BIFs (Bekker et al., 2010).

A high Si-Fe(III)(oxyhydr)oxide content, absence of carbonate and sulfide mineralization, coupled to a generally low S content have also been demonstrated for the CVSB Fe formations (Chi Fru et al., 2013, 2015). This depositional situation is different, for example, from the unconfined shallow submarine hydrothermal systems in Tatum Bay and Bahia Concepcion Bahia Carlifornia Sur, Mexico, where authigenic carbonate deposition is widespread (Canet et al., 2005; Pichler & Veizer, 1996, 2005). Moreover, there is strong geological evidence that within volcanic crater environments associated with high CO<sub>2</sub> emission, long-term water column redox stratification is possible under these special conditions. Further evidence is found in volcanic crater lakes (for example the shallow 205 m deep lake Nyos in Cameroon—renowned as one of Earth's three CO<sub>2</sub> saturated volcanic lakes (Ozawa et al., 2016; Kling et al., 2005). Here CO<sub>2</sub>-induced water column stratification is associated with bottom reducing conditions characterized by a low sulfate and high Fe bottom water content relative to surface concentrations (Tiodjio et al., 2014).

## 5 Concluding remarks

This study shows the following new insights in light of what was previously known:

Ernest Chi Fru 22/2/2018 10:08

**Deleted:** Moreover, the anoxic amorphous Si-Fe(III)(oxyhydr)oxide-rich-sulfide-poor shallow submarine environments at Kameni islands, have been independently proposed as a modern analogue environment for Precambrian BIF precipitation (Hanert, 2002; Robbins et al., 2016).

1. At least two distinct IFs (MFIF and NFIF) formed from hydrothermal mud, within two localized sub-basins in the ~1 km-long CVSB, ~2.66-1.0 Myr ago, controlled by local tectonism.
2. Local conditions of elevated and cyclic supply of ferrous Fe and dissolved Si, accompanied by strict bottom water anoxic conditions in a localized reservoir cut off from the open ocean, can in principle allow the deposition of BIF-type rocks in a modern marine setting. The rarity of these types of deposits however suggests that such conditions are extremely difficult to attain under the modern oxygen-rich atmosphere.
3. A working model that band formation may involve potential Fe(III)(oxyhydr)oxide filling of sediment pores and fractures during diagenesis, is not supported by the data. In addition to the lack of observation of such phenomena, as demonstrated for replacive Mn mineralization, calculated Ce and Eu anomalies, together with preliminary sequential iron extraction analysis (Poulton and Canfield, 2011; data not shown), are suggestive of anoxic depositional conditions likely induced by the release of reduced hydrothermal/volcanic fluids into a cutoff sedimentary basin.
4. The precipitation of Fe(III) and Mn oxides require oxygen. In the absence of oxygen, Mn is not oxidized, while light and photoferrotrophy will oxidize reduced Fe to Fe(III)(oxyhydr)oxides. Both light and photoferrotrophy are however extremely rare characteristics of anoxic sediments, but a common feature of anoxic Fe<sup>2+</sup>-rich waters, where photoferrotrophy is widespread (Weber et al., 2006). Collectively, these observations provide an important feasible mechanism for the knife sharp separation of the Mn oxide-rich ores in the CVSB that are also Fe(III)(oxyhydr)oxide-rich, from the highly

1191 localized MFIF and NFIF deposits that are Fe(III)(oxyhydr)oxide-rich but Mn  
1192 oxide-poor.

1193 5. The mechanism of formation of the MFIF and NFIF therefore most likely  
1194 involved exhalative release of reduced hydrothermal/volcanic fluids into a  
1195 restricted and deoxygenated seafloor water column where the oxidation of  
1196 reduced Fe to Fe(III)(oxyhydr)oxides occurred, most likely by the activity of  
1197 photoferrotrophs (Chi Fru et al., 2013). [Microaerophilic oxidation of Fe\(II\)](#)  
1198 [was likely critical, but that remains to be shown.](#)

1199 6. Episodic intensification of hydrothermal activity is identified as a main  
1200 mechanism for the formation of the millimetric BIF bands, adding to the  
1201 biological mechanism that was inferred from fossil records in the MFIF (Chi  
1202 Fru et al., 2013, 2015).

1203 7. Abiotic Si precipitation was apparently much slower relative to Fe(III)  
1204 precipitation, resulting in Fe-rich bands in the NFIF forming in association  
1205 with large fragments of volcaniclast and the Si-rich bands with finer Si grains.

1206 8. A combination of the above processes produced pulses of Si and Fe in the  
1207 millimetric Si and Fe-rich bands in the NFIF.

1208 9. The Milos rocks fulfill sedimentological, chemical and mineralogical  
1209 characteristics that established them as potentially the youngest known BIFs;  
1210 following the simplistic definition that BIFs are sedimentary rocks composed  
1211 of alternating layers of Fe and Si containing at least 15% Fe.

1212 10. Whether the rocks described here are analogues of Precambrian BIFs or not,  
1213 and whether the proposed formation mechanisms match those that formed the  
1214 ancient rocks, is opened to debate. [However, there are many similarities to](#)  
1215 [proposed Precambrian BIF depositional models \(e.g. Klien, 2005; Beukes and](#)

1216 [Gutzmer, 2008; Smith et al., 2013; Bekker et al., 2010; Klein and Beukes,](#)  
1217 [1992\).](#) **Importantly**, the present study provides mechanisms by which rocks  
1218 with alternating Fe and Si-rich bands can be formed in the modern ocean.

1219

1220 *Data availability.* Data can be accessed by request from any of the authors

1221

1222 *Author contributions.* ECF, SK and MI designed the study. ECF, SK, KG and MI  
1223 performed fieldwork. ECF, JER, KG, IM and QH performed research. ECF, SK, KG,  
1224 MI, QH and JER interpreted data. ECF and SK wrote paper.

1225

1226 *Competing interests.* The authors declare that they have no conflict of interest.

1227

1228 *Acknowledgments.* Ariadne Argyraki, Nicole Posth, Nolwenn Callac and Eva Zygouri  
1229 are acknowledged field assistance during sampling and for stimulating intellectual  
1230 discussions. Special thanks to Christoffer Hemmingsson for contributing to the SEM  
1231 and XRD analyses. This work is funded by the European Research Council grant No.  
1232 336092 to ECF and the Swedish Research Council grant No. 2012-4364 to MI.

1233

1234

## 1235 **References**

1236 Alain, K., Holler, T., Musat, F., Elvert, M., Treude, T., and Kruger M.;  
1237 Microbiological investigation of methane- and hydrocarbon-discharging mud  
1238 volcanoes in the Carpathian Mountains, Romania. Environ. Microbiol., 8, 574–  
1239 590, 2006.



- 1240 Alfieris, D. and Voudouris, P.: Ore mineralogy of transitional submarine magmatic-  
1241 hydrothermal deposits in W. Milos Island, Greece. *Bul. Acad. Sci.*, 43, 1–6, 2005.
- 1242 Alfieris, D.: Geological, geochemical and mineralogical studies of shallow submarine  
1243 epithermal mineralization in an emergent volcanic edifice, at Milos Island (western  
1244 side), Greece. PhD thesis, Department Geowissenschaften der Universität  
1245 Hamburg, 2006.
- 1246 Alfieris, D., Voudouris, P., and Spry, P.: Shallow submarine epithermal Pb–Zn–Cu–  
1247 Au–Ag–Te mineralization on western Milos Island, Aegean Volcanic Arc, Greece:  
1248 Mineralogical, geological and geochemical constraints. *Ore Geol. Rev.*, 53, 159–  
1249 180, 2013.
- 1250 Anand, R. R., Paine, M., and Smith, R.E.: Genesis, Classification and Atlas of  
1251 Ferruginous Materials, Yilgarn Craton. CRC LEME Open File Report vol. 13,  
1252 CSIRO Exploration and Mining, Perth, 2002.
- 1253 Bahlburg, H. and Dobrzinski, N.: A review of the Chemical Index of Alteration (CIA)  
1254 and its application to the study of Neoproterozoic glacial deposits and climate  
1255 transition. *Geol. Soc. London Mem.*, 36, 81–92, 2011.
- 1256 Bau, M. and Dulski, P.: Distribution of yttrium and rare- earth elements in the Penge  
1257 and Kuruman Iron-Formations, oxidative scavenging of cerium on hydrous Fe  
1258 oxide, Transvaal Supergroup, South Africa. *Precambrian Res.*, 79, 37–55, 1996.
- 1259 Berg, I.A., Kockelkorn, D., Ramos-Vera, W.H., Say, R.F., Zarzycki, J., Hügler, M.,  
1260 Alber, B.E., and Fuchs, G.: Autotrophic carbon fixation in archaea. *Nat. Rev.*  
1261 *Microbiol.*, 8, 447–460, 2010.
- 1262 Bekker, A., Slack J.F., Planavsky, N., Krapež B., Hofmann, A., Konhauser, K.O., and  
1263 Rouxel, O.J.: Iron formation: The sedimentary product of a complex interplay

1264 among mantle, tectonic, oceanic, and biospheric processes. *Econ. Geol.*, 105, 467–  
 1265 508, 2010.

1266 [Beukes, N.J., and Gutzmer, J.: Origin and Paleoenvironmental significance of major](#)  
 1267 [Iron Formations at the Archean-Paleoproterozoic boundary. \*Econ. Geol.\* 15, 5–47,](#)  
 1268 [2008.](#)

1269 [Beukes, N.J., Swindell, E.P.W., Wabo, H.: Manganese deposits of Africa, Episodes v.](#)  
 1270 [39, 285–317, 2016.](#)

1271 [Blumenberg, M., Seifert, R., Reitner, J., Pape, T., and Michaelis, W.: Membrane lipid](#)  
 1272 [patterns typify distinct anaerobic methanotrophic consortia. \*Proc. Natl. Acad. Sci.\*](#)  
 1273 [U.S.A., 101, 11111–11116, 2004.](#)

1274 Boström, K., Honnorez, J., Joensuu, O., and Rydell, H.: Chemistry of hydrothermal  
 1275 solutions in drill hole GPK-1, Palaea Kameni, Santorini, Greece. *Proceedings of*  
 1276 *the third international congress, Santorini, Greece.* 3, 257–260, 1990.

1277 Bronn, H.G.: *Übersicht der Fossilen Überreste in den tertiären subappenninischen*  
 1278 *Gebirgen. Italiens Tertiär-Gebilde und deren organische Einschlüsse.* Heidelberg  
 1279 pp. XII + 176 + 1 pl, 1831.

1280 Bouma, A.H.: *Sedimentology of Some Flysch Deposits.* Amsterdam, Elsevier, pp.  
 1281 168, 1962.

1282 Breitreuz, C.: Spherulites and lithophysae—200 years of investigation on  
 1283 hightemperature crystallization domains in silica-rich volcanic rocks. *Bull.*  
 1284 *Volcanol.*, 75, 1–16, 2013.

1285 Bühring, S.I., Elvert, M., and Witte, U.: The microbial community structure of  
 1286 different permeable sandy sediments characterized by the investigation of bacterial  
 1287 fatty acids and fluorescence in situ hybridization. *Environ. Microbiol.*, 7, 281–293,  
 1288 2005.

Ernest Chi Fru 26/2/2018 10:55

**Deleted:** Beukes, N. J. and Klein, C.: Geochemistry and sedimentology of a facies transition—from microbanded to granular iron-formation—in the early Proterozoic Transvaal Supergroup, South Africa. *Pre. Res.*, 47, 99–139, 1990. .

1295 Camilli, R., Noumikou P., Escartin, J., Ridao, P., Mallios, A., Kiliass, S.P., Argyraki,  
 1296 A., and the Caldera Science Team: The Kallisti Limnes, carbon dioxide  
 1297 accumulating subsea pools. *Sci. Rep.*, 5, 12152, doi:10.1038/srep12152.  
 1298 Canuel, E.A. and Marten, C.S.: Reactivity of recently deposited organic matter:  
 1299 Degradation of lipid compounds near the sediment-water interface. *Geochim.*  
 1300 *Cosmo. Acta*, 60, 1793–1806, 1996.  
 1301 Canet, C., Prol-Ledesma, R.M., Torres-Alvarado, I., Gilg, H.A., Villanueva, R.E., and  
 1302 Cruz, R.L.S.: Silica-carbonate stromatolites related to coastal hydrothermal venting  
 1303 in Bahia Concepcion, Baja California Sur, Mexico. *Sed. Geol.*, 174, 97–113, 2005.  
 1304 Cattaneo, A. and Steel, R.J.: Transgressive deposits: a review of their variability.  
 1305 *Earth Sci. Rev.*, 62, 187–228, 2003.  
 1306 Chi Fru, E., Ivarsson, M., Kiliass, S.P., Bengtson, S., Belivanova, V., Marone, F.,  
 1307 Fortin, D., Broman, C., and Stampanoni, M.: Fossilized iron bacteria reveal a  
 1308 pathway to the origin banded iron formations. *Nat. Comm.*, 4, 2050 DOI:  
 1309 10.1038/ncomms3050, 2013.  
 1310 Chi Fru, E., Ivarsson, M., Kiliass, S.P., Frings, P.J., Hemmingsson, C., Broman, C.,  
 1311 Bengtson, S. and Chatzitheodoridis, E.: Biogenicity of an Early Quaternary iron  
 1312 formation, Milos Island, Greece. *Geobiology*, 13, 225–44, 2015.  
 1313 Dando, P.R., Hughes, J.A., Leahy, Y., Niven, S.J., Taylor, L.J. and Smith, C.: Gas  
 1314 venting rates from submarine hydrothermal areas around the island of Milos,  
 1315 Hellenic Volcanic Arc. *Cont. Shelf Res.*, 15, 913–925, 1995.  
 1316 Dieke, P. Concentration of Mn and separation from Fe in sediments—I.  
 1317 Kinetics and stoichiometry of the reaction between birnessite and  
 1318 dissolved Fe(II) at 10°C. *Geochim. Cosmo. Acta*, 49, 1023–1033, 1985.

1319 Dorr, J.V.N.: Supergene iron ores of Minas Gerais, Brazil. *Econ. Geol.*, 59, 1203,  
1320 1964.

1321 Dowling, N.J. E., Widdel, F., and White, D.C.: Phospholipid ester-linked fatty-acid  
1322 biomarkers of acetate-oxidizing sulfate-reducers and other sulfide-forming  
1323 bacteria. *J. Gen. Microbiol.*, 132, 1815–1825, 1986.

1324 Druitt, T. H. L., Edwards, R. M., Mellors, D. M., Pyle, R. S. J., Sparks, M., Lanphere,  
1325 M. D., and Barreirio, B.: Santorini Volcano. *Geol. Soc. Mem. London*, 19, 165,  
1326 1999.

1327 Fischer, W.W. and Knoll, A.H.: An iron shuttle for deepwater silica in Late Archean  
1328 and early Paleoproterozoic iron formation. *Geol. Soc. Am. Bull.*, 121, 222–235,  
1329 2009.

1330 Franco, A.C., Hernández-Ayón, J.M, Beier E., Garçon, V., Maske, H., Paulmier, A.,  
1331 Färber-Lorda, J., Castro, R., and Sosa-Ávalos, R.: Air-sea CO<sub>2</sub> fluxes above the  
1332 stratified oxygen minimum zone in the coastal region off Mexico. *J. Geophys. Res.*,  
1333 119, 2923–2937, 2014.

1334 Friedrich, W.L., Kromer, B., Friedrich, M., Heinemeier, J., Pfeiffer, T., and Talamo,  
1335 S.: Santorini eruption radiocarbon dated to 1627-1600 BC. *Science*, 312, 548–548,  
1336 2006.

1337 [Fytikas, M., Innocenti, F., Kolios, N., Manetti, P., Mazzuoli, R., Poli, G., Rita, F., and](#)  
1338 [Villari, L.: Volcanology and petrology of volcanic products from the island of](#)  
1339 [Milos and Neighbouring islets. \*J. Vol. Geotherm. Res.\*, 28, 297–317, 1986.](#)

1340 Galan, L.D.P., Doval, M., La Iglesia, A., Soriano, J., and Chavez, L.: Occurrence of  
1341 silica polymorphs nanocrystals in tuffaceous rocks, Province of the Mesa Central,  
1342 Mexico, and their formation from subcritical Si-rich fluids. *Am. Mineral.*, 98, 977–  
1343 985, 2013.

- 1344 Georgalas, G., and Liatsikas, N.: Die Historische entwicklung des Dafni-Ausbruches  
 1345 1925-1926. In Santorin, Der Werdegang eines Inselvulkans und sein Ausbruch  
 1346 1925-1928, V. 2 (ed. Reck, H.). Verlag von Dietrich Reimer, Berlin, 1–96 pp,  
 1347 1936.
- 1348 Glasby, G.P. and Schulz, H.D.: Eh, pH diagrams for Mn, Fe, Co, Ni, Cu and As under  
 1349 seawater conditions: application of two new types of the Eh, pH diagrams to the  
 1350 study of specific problems in marine geochemistry. *Aquatic Geochem.*, 5, 227–  
 1351 248, 1999.
- 1352 Glasby, G.P., Papavassiliou, C.T., Mitsis, J., and Valsami-Jones, E.: The Vani  
 1353 manganese deposit, Milos island, Greece: A fossil stratabound  
 1354 Mn–Ba–Pb–Zn–As–Sb–W-rich hydrothermal deposit. *Develop. Volcanol.*, 7,  
 1355 255–291, 2005.
- 1356 Gromet, L.P., Dymek, R.F., Haskin, L.A., and Korotev, R.L.: The North American  
 1357 shale composi: Its compilation and major trace element characteristics. *Geochim.*  
 1358 *Cosmo. Acta*, 48, 2469–2482, 1984.
- 1359 Gross, G.A.: A classification of iron-formation based on depositional Environments.  
 1360 *Can. Min.*, 18, 215–222, 1980.
- 1361 Guilbaud, R., Poulton, S.W., Butterfield, N.J., Zhu, M., and Shields-Zou, G.A.: A  
 1362 global transition to ferruginous conditions during the early Neoproterozoic. *Nat.*  
 1363 *Geosci.* 8:466–470, 2015.
- 1364 Handley, K. M., Boothman, C., Mills, R. A., Pancost, R. D., and Lloyd, J. R.:  
 1365 Functional diversity of bacteria in a ferruginous hydrothermal sediment. *ISME J.*,  
 1366 4, 1193-1205, 2010.

Ernest Chi Fru 23/2/2018 20:15

**Deleted:** Han, C., Xiao, W., Su, B., Chen, Z., Zhang, X., Ao, S., Zhang, J., Zhang, Z., Wan, B., Song, D., and Wang, Z.: Neoproterozoic Algoma-type banded iron formations from Eastern Hebei, North China Craton: SHRIMP U-Pb age, origin and tectonic setting. *Precam. Res.*, 251, 212–231, 2014. .

1375 Hanert, H. H.: Bacterial and chemical iron oxide deposition in a shallow bay on  
 1376 Palaea Kameni, Santorini, Greece: microscopy, electron probe microanalysis, and  
 1377 photometry of in situ experiments. *Geomicrobiol. J.*, 19, 317–342, 2002.

1378 | [Hein, J. R., Stamatakis, M. G., and Dowling, J. S.: Trace metal-rich Quaternary](#)  
 1379 hydrothermal manganese oxide and barite deposit, Milos Island, Greece. *Applied*  
 1380 *Earth Science: Trans. Inst. Min. Metal. Section B.*, 109, 67–76, 2000.

1381 | [Horwell, C.J., le Blond, S., Michnowicz, S. A. K. and Cressey, G.: Cristobalite in a](#)  
 1382 rhyolitic lava dome: evolution of ash hazard. *Bull. Volcanol.* 72, 249-253, 2010.

1383 Ichihara, K. and Fukubayashi, Y.: Preparation of fatty acid methyl esters for gas-  
 1384 liquid chromatography. *J. Lipid Res.*, 51, 635–40, 2010.

1385 James, H. L.: Sedimentary facies of iron-formation. *Econ. Geol.*, 49, 235–293, 1954.

1386 | [Johnson, C. M., Beard, B. L., and Roden, E. E.: The iron isotope fingerprints of redox](#)  
 1387 and biogeochemical cycling in modern and ancient Earth. *Ann. Rev. Earth Plan.*  
 1388 *Sci.*, 36, 457–493, 2008.

1389 Kappler, A., Pasquero, C., and Newman, D.K.: Deposition of banded iron formations  
 1390 by anoxygenic phototrophic Fe(II)-oxidizing bacteria. *Geology*, 33, 865–868,  
 1391 2005.

1392 Kilias, S. P., Detsi, K., Godelitsas, A., Typas, M., Naden, J., and Marantos, Y.:  
 1393 Evidence of Mn-oxide biomineralization, Vani Mn deposit, Milos, Greece. In:  
 1394 Proceedings of the ninth biennial Meeting of the Society for Geology Applied to  
 1395 Mineral Deposits, Dublin, Ireland. *Irish Assoc. Econ. Geol.* 1069–1072 pp, 2007.

1396 Kilias, S. P.: Microbial mat-related structures in the Quaternary Cape Vani  
 1397 manganese-oxide (-barite) deposit, NW Milos island, Greece. *Soc. Sed. Geol. Sp.*  
 1398 *Pub.*, 101, 97–110, 2011.

Ernest Chi Fru 23/2/2018 20:16

**Deleted:** Hein, J. R. and Conrad, T. A.: Copper-nickel-rich, amalgamated ferromanganese crust-nodule deposits from Shatsky Rise, NW Pacific. *Geochem. Geophys. Geosyst.*, 13, Q10022, doi:10.1029/2012GC004286, 2012. .

Ernest Chi Fru 23/2/2018 20:17

**Deleted:** Hickman, A.H.: Regional review of the 34236–3350 Ma Strelley Pool Formation, Pilbara Craton, Western Australia. *Geol Survey West Australia*, 215, 1-23, 2008. .

Ernest Chi Fru 23/2/2018 20:18

**Deleted:** James, H. L.: Distribution of banded iron-formation in space and time. *Dev. Pre. Geol.*, 6, 471–490, 1983. .

1412 Kilias, S. P., Chatzitheodoridis, E., and Lyon, I.: Molecular, chemical and  
 1413 morphological evidence for hematite biogenicity at the Quaternary Cape Vani Mn-  
 1414 (Ba-Fe) deposit, Milos, Greece. *Bull. Geol. Soc.*, 47, 834-842, 2013a.

1415 Kilias, P. S., Nomikou, P., Papanikolaou, D., Polymenakou, P. N., Godelitsas, A.,  
 1416 Argyraki, A., Carey, S., Gamaletsos, P., Mertzimekis, T. J., Stathopoulou, E.,  
 1417 Goettlicher, J., Steininger, R., Betzelou, K., Livanos, I., Christakis, C., Bell, K. C.:  
 1418 and Scoullou, M. New insights into hydrothermal vent processes in the unique  
 1419 shallow-submarine arc-volcano, Kolumbo (Santorini), Greece. *Sci. Rep.*, 3,  
 1420 doi:10.1038/srep02421, 2013b.

1421 Klein, C.: Some Precambrian banded iron-formations (BIFs) from around the world:  
 1422 Their age, geologic setting, mineralogy, metamorphism, geochemistry, and origins.  
 1423 *Am. Min.*, 90, 1473–1499, 2005.

1424 Kling, G. W., Evans, W. C., Tanyileke, G., Kusakabe, M., Ohba, T., Yoshida, Y., and  
 1425 Hell, J. V.: Degassing Lakes Nyos and Monoun: Defusing certain disaster. *Proc.*  
 1426 *Natl. Acad. Sci. U.S.A.*, 102, 14185–14190, 2005.

1427 [Klein, C., and Beukes, N.J.: Time distribution, stratigraphy and sedimentologic](#)  
 1428 [setting, and geochemistry of Precambrian Iron Formation. In Schopf, J. W., and](#)  
 1429 [Klein, C.: The Proterozoic Biosphere: A multidisciplinary study, 139 – 146.](#)  
 1430 [Cambridge University Press, New York, 1992.](#)

1431 Konhauser, K. O., Planavsky, N. J., Hardisty, D. S., Robbins, L. J., Warchola, T. J.,  
 1432 Haugaard, R., Lalonde, S. V., Partin, C. A., Oonk, P. B. H., Tsikos, H., and Lyons,  
 1433 T.W.: Iron formations: A global record of Neoproterozoic to Palaeoproterozoic  
 1434 environmental history. *Earth Sci. Rev.*, 172, 140-177, 2017.

1435 [Krapež, B., Barley, M. E., Pickard, A. L.: Hydrothermal and resedimented origins of](#)  
 1436 [the precursor sediments to banded iron formations: Sedimentological evidence](#)

Ernest Chi Fru 23/2/2018 20:22

**Deleted:** Konhauser, K. O., Hamade, T., Riaswell, R., Morris, R. C., Ferris, F. G., Southam, G. and Canfield, D. E.: Could bacteria have formed the Precambrian banded iron formations? *Geology*, 12, 1097–1082, 2002. .

1443 from the early Palaeoproterozoic Brockman Supersequence of Western Australia.  
 1444 Sedimentology, 50, 979-1011, 2003.

1445 Lalonde, K., Mucci, A., Quellet, A. and G  linas, Y.: Preservation of organic matter in  
 1446 sediments promoted by iron. Nature, 483, 198–200, 2012.

1447 Levett, A., Gagen, E., Shuster, J., Rintoul, L., Tobin, M., Vongsivut, J., Bambery,  
 1448 K., Vasconcelos, P., and Southam, G.: Evidence of biogeochemical processes in  
 1449 iron duricrust formation. J. South. Am. Earth Sci., 71, 131–142, 2016.

1450 Li, W., Czaja, A. D., Van Kranendonk, M. J., Beard, B. L., Roden, E. E., Johnson, C.  
 1451 M.: An anoxic, Fe(II)-rich, U-poor ocean 3.46 billion years ago. Geochim. Cosmo.  
 1452 Acta, 120, 65-79, 2013.

1453 Liakopoulos, A., Glasby, G. P., Papavassiliou, C. T. and Boulegue, J.: Nature and  
 1454 origin of the Vani manganese deposit, Milos, Greece: an overview. Ore Geol. Rev.,  
 1455 18, 181–209, 2001.

1456 [L  , D., Song, Q., and Wang, X.: Decomposition of algal lipids in clay-enriched](#)  
 1457 [marine sediment under oxic and anoxic conditions. Chin. J. Oceanogr. Limnol., 28,](#)  
 1458 [131–143, 2010.](#)

1459 Marschik, R., Bauer, T., Hensler, A.-S., Skarpelis, N., and H  lzl, S. Isotope  
 1460 Geochemistry of the Pb-Zn-Ba(-Ag-Au) Mineralization at Triades-Galana, Milos  
 1461 Island, Greece. Res. Geol., 60, 335–347, 2010.

1462 Maynard, J. B.: Chemistry of modern soils as a guide to interpreting Precambrian  
 1463 Paleosols. J. Geol., 100, 279–289, 1993.

1464 Maynard, J. B.: The chemistry of manganese ores through time: a signal of increasing  
 1465 diversity of earth-surface environments. Econ. Geol., 105, 535–552, 2010.

1466 [McLennan, S.B.: Rare earth elements in sedimentary rocks. Influence of provenance](#)  
 1467 [and sedimentary processes. In: B.R. Lipin and G.A. McKay \(Editors\),](#)

Ernest C 23/2/2018 13:35

**Deleted:** Lowe, D.R.: Sediment gravity flows: II. Depositional models with special reference to the deposits of high-density turbidity currents. J. Sed. Petrol., 52, 279–297, 1982. .

... [2]



1474 | [Geochemistry and Mineralogy of the Rare Earth Elements. Mineralogical Society](#)  
 1475 | [of America, Washington, pp. 169-200, 1989.](#)  
 1476 | Miall, A. D. Lithofacies types and vertical profile models in braided river deposits.  
 1477 | Can. Soc. Pet. Geol. Mem., 5, 597–604, 1978.  
 1478 | Miall, A. D.: Architectural element analysis: a new method of facies analysis applied  
 1479 | to fluvial deposits. Earth Sci. Rev., 22, 261e308, 1985.  
 1480 | Morris, R. V., Vaniman, D. T., Blake, D. F., Gellert, R., Chipera, S. J., Rampe, E. B.,  
 1481 | Ming, D. W., Morrison, S. M., Downs, R. T., Treiman, A. H., Yen, A. S.,  
 1482 | Grotzinger, J. P., Achilles, C. N., Bristow, T. F., Crisp, J. A., Des Marais, D. J.,  
 1483 | Farmer, J. D., Fendrich, K. V., Frydenvang, J., Gradd, T. G., Morookian, J-M.,  
 1484 | Stolper, E. M. and Schwenzer, S. P.: Silicic volcanism on Mars evidenced by  
 1485 | tridymite in high-SiO<sub>2</sub> sedimentary rock at Gale crater. Proc. Natl. Acad. Sci.  
 1486 | U.S.A., 113, 7071–7076, 2016.  
 1487 | Mutti, E.: Turbidite Sandstones. Agip Spe. Pub., 275 pp, 1992.  
 1488 | Nesbitt, H. W. and Young, G. M.: Early Proterozoic climates and plate motions  
 1489 | inferred from major element chemistry of lutites. Nature, 199, 715–717, 1982.  
 1490 | [Nomikou, P., Papanikolaou, D., Alexandri, M., Sakellariou, D., and Rousakis, G.:](#)  
 1491 | Submarine volcanoes along the Aegean volcanic arc. Tectonophysics, 597–598,  
 1492 | 123–146, 2013.  
 1493 | Nomikou, P., Parks, M. M., Papanikolaou, D., Pyle, D. M., Mather, T. A., Carey, S.,  
 1494 | Watts, A. B., Paulatto, M., Kalnins, M.L., Livanos, I., and Bejelou, K.: The  
 1495 | emergence and growth of a submarine volcano: The Kameni islands, Santorini  
 1496 | (Greece). Geo. Res. J., 1, 8–18, 2014.

Ernest Chi Fru 23/2/2018 20:29

**Deleted:** Nijman, W., De Bruin, K., and  
 Valkering, M.: Growth fault control of early  
 Archean cherts, barite mounds, and chert-  
 barite veins, North Pole Dome, Eastern  
 Pilbara, Western Australia. Precam. Res., 88,  
 25–52, 1998. ... [3]

1504 | Ozawa, A., Ueda, A., Fantong, W. Y., Anazawa, K., Yoshida, Y., Kusakabe, M.,  
 1505 | Ohba, T., Tanyileke, G., and Hell, J.V. Rate of siderite precipitation in Lake Nyos,  
 1506 | Cameroon. *Geol. Soc. London Sp. Pub.*, 437, doi.org/10.1144/SP437.13, 2016.  
 1507 | Papanikolaou, D., Lekkas, E., and Syskakis, D.: Tectonic analysis of the geothermal  
 1508 | field of Milos Island. *Bull. Geol. Soc. Greece*, 24, 27–46, 1990.  
 1509 | Papavassiliou, K., Voudouris, P., Kanellopoulos, C., Glasby, G., Alfieris, D., and  
 1510 | Mitsis, I.: New geochemical and mineralogical constraints on the genesis of the  
 1511 | Vani hydrothermal manganese deposit at NW Milos island, Greece: Comparison  
 1512 | with the Aspro Gialoudi deposit and implications for the formation of the Milos  
 1513 | manganese mineralization. *Ore Geol.*, 80, 594–611, 2017.  
 1514 | Paulmier, A., Ruiz-Pino, D., and Garçon, V.: The oxygen minimum zone (OMZ) off  
 1515 | Chile as intense source of CO<sub>2</sub> and N<sub>2</sub>O, *Cont. Shelf. Res.*, 28, 2746–2756, 2008.  
 1516 | Paulmier, A., Ruiz-Pino, D., and Gaçon, V.: CO<sub>2</sub> maximum in the oxygen minimum  
 1517 | zone (OMZ). *Biogeosciences*, 8, 239–252. doi:10.5194/bg-8-239-2011, 2011.  
 1518 | Percoits, E., Gingras, M. K., Barley, M. E., Kapper, A., Posth, N. R., and Konhauser,  
 1519 | K.O.: Petrography and geochemistry of the Dales Gorge banded iron formation:  
 1520 | Paragenetic sequence, source and implications for palaeo-ocean chemistry. *Pre.*  
 1521 | *Res.*, 172, 2009.  
 1522 | Pichler, T. and Dix, G. R. Hydrothermal venting within a coral reef ecosystem,  
 1523 | Ambitle Island, Papua New Guinea. *Geology*, 50, 435–438, 1996.  
 1524 | Pichler, T. and Veizer, J.: Precipitation of Fe(III) oxyhydroxide deposits from  
 1525 | shallow-water hydrothermal fluids in Tutum Bay, Ambitle Island, Papua New  
 1526 | Guinea. *Chem. Geol.*, 162, 15–31, 1999.

Ernest Chi Fru 23/2/2018 20:30

**Deleted:** Ossa, F. O., Hofmann, A., Vidal, O., Kramers, J. D., Belyanin, G. and Cavalazzi, B.: Unusual manganese enrichment in the Mesoarchean Mozaan Group, Pongola Supergroup, South Africa. *Pre. Res.*, 281, 414–433, 2016. ↗

Ernest Chi Fru 23/2/2018 20:31

**Deleted:** Papike, J. J., Karner, J. M., Shearer, C. K. and Burger, P. V.: Silicate mineralogy of martian meteorites. *Geochim. Cosmochim. Acta*, 73, 7443–7485, 2009. ↗

1537 Pichler, T. and Veizer, J. The precipitation of aragonite from shallow-water  
 1538 hydrothermal fluids in a coral reef, Tutum Bay, Ambitle Island, Papua New  
 1539 Guinea. *Chem. Geol.*, 207, 317–45, 2004.

1540 Planavsky, N., Rouxel, O., Bekker, A., Shapiro, R., Fralick, P., and Knudsen, A.:  
 1541 Iron-oxidizing microbial ecosystems thrived in late Paleoproterozoic redox-  
 1542 stratified oceans. *Earth Plan. Sci. Letts.*, 286, 2307–242, 2009.

1543 Planavsky, N. J., Bekker, A., Rouxel, O. J., Kamber, B., Hofmann, A., Knudsen, A.  
 1544 and Lyons T. W.: Rare earth element and yttrium compositions of Archean and  
 1545 Paleoproterozoic Fe formations revisited: New perspectives on the significance  
 1546 and mechanisms of deposition. *Geochim. Cosmo. Acta*, 74, 6387–6405, 2010.

1547 Plimer, I. *Milos Geologic History*. Koan Publishing House, Athens, Greece. 261 pp,  
 1548 2000.

1549 Poulton, S.W., and Canfield, D.E.: Development of a sequential iron extraction  
 1550 procedure for iron: implications for iron partitioning in continentally derived  
 1551 particles. *Chem. Geol.* 2014, 209–221, 2005.

1552 Poulton, S.W. and Canfield, D.E.: Ferruginous conditions: A dominant feature of the  
 1553 ocean through Earth's history. *Elements*. 7, 107–112, 2011.

1554 Preuß, A., Schauder, R., Fuchs, G., and Stichler W.: Carbon isotope fractionation by  
 1555 autotrophic bacteria with three different CO<sub>2</sub> fixation pathways. *Zeitschrift für*  
 1556 *Naturforschung C.*, 44, 397–402, 1989.

1557 Rancourt, D. G., Fortin, D., Pichler, T., and Lamarche, G.: Mineralogical  
 1558 characterization of a natural very As-rich hydrous ferric oxide coprecipitate formed  
 1559 by mixing of hydrothermal fluid and sea water. *Am. Min.*, 86, 834–851, 2001.

Ernest Chi Fru 23/2/2018 20:38

**Deleted:** Ramos, E., Marzo, M., de Gibert, J. M., Tawengi, K. S., Khoja, A. A., and Bolatti, N. D.: Stratigraphy and sedimentology of the middle Ordovician Hawaz formation (Murzuq Basin, Libya). *AAPG bull.*, 90, 1309-1336, 2006. -

1566 Rasmussen, B., Meier, D. B., Krapež. B., and Muhling, J. R.: Iron silicate  
 1567 microgranules as precursor sediments to 2.5-billion-year-old banded iron  
 1568 formations. *Geology*, 41, 435–438, 2013.

1569 Rasmussen, B., Krapež, B., and Meier, D. B. Replacement origin for hematite in 2.5  
 1570 Ga banded iron formation: Evidence for postdepositional oxidation of iron-bearing  
 1571 minerals. *Geol. Soc. Am. Bull.*, 126, 438–446, 2014.

1572 Riedel, T., Zak, D., Biester, H., and Dittmar, T.: Iron traps terrestrially derived  
 1573 dissolved organic matter at redox interfaces. *Proc. Nat. Acad. Sci. U.S.A.*, 110,  
 1574 10101–10105, 2013.

1575 Robbins, E. I., Kourtidou-Papadeli, C., Iberall, A. S., Nord, Jr, G. L. and Sato, M.:  
 1576 From Precambrian Iron-Formation to Terraforming Mars: The JIMES Expedition  
 1577 to Santorini. *Geomicrobiol. J.*, 33, 630–645, 2016.

1578 Roy, S.: Manganese Mineralization: Geochemistry and mineralogy of terrestrial and  
 1579 marine deposits. *Geol. Soc. Spe. Pub.*, 119, 5–27, 1997.

1580 Roy, S.: Sedimentary manganese metallogenesis in response to the evolution of the  
 1581 Earth system. *Earth-Sci. Rev.*, 77, 273–305, 2006.

1582 Rudnick, R. and Gao, S. Composition of the continental crust. In: *Treatise on*  
 1583 *Geochemistry*, vol. 3. Elsevier–Pergamon, Oxford, 1–64 pp, 2003.

1584 Shanmugam, G.: Submarine fans: a critical retrospective (1950–2015). *J.*  
 1585 *Palaeogeogr.*, 5, 110–184, 2016.

1586 Schwertmann, U. and Murad, E. Effect of pH on the formation of goethite and  
 1587 hematite from ferrihydrite. *Clay Clay Min.*, 31, 277–284, 1983.

1588 Shuster, D. L., Farley, K. A., Vasconcelos, P. M., Balco, G., Monteiro, H. S.,  
 1589 Waltenberg, K., and Stone, J. O. Cosmogenic  $^3\text{He}$  in hematite and goethite from

1590 Brazilian “canga” duricrust demonstrates the extreme stability of these surfaces.  
 1591 Earth Plan. Sci. Lett., 329, 41–50, 2012.

1592 Sigurdsson, H., Carey, S., Alexandri, M., Vougioukalakis, G., Croff, K., Roman, C.,  
 1593 Sakellariou, D., Anagnostou, C., Rousakis, G., Loakim, C., Goguo, A., Ballas, D.,  
 1594 Misaridis, T., and Nomikou, P. Marine investigations of Greece’s Santorini  
 1595 volcanic field. EOS Trans. Am. Geophy. Union, 87, 337–342, 2006.

1596 Simonson, B. M.: Sedimentological constraints on the origins of Precambrian iron-  
 1597 formations. Geol. Soc. Am. Bull., 96, 244–252, 1985.

1598 [Simonson, B. M. and Hassler, S. W.: Was the deposition of large Precambrian iron](#)  
 1599 [formations linked to major marine transgressions? The J. Geol., 104, 665–676,](#)  
 1600 [1996.](#)

1601 Skarpelis, N. and Koutles, T.: Geology of epithermal mineralization of the NW part of  
 1602 Milos Island, Greece. In Proceedings of the 5th International Symposium on  
 1603 Eastern Mediterranean Geology. (eds. Chatzipetros, A. & Pavlides S). School of  
 1604 Geology, Aristotelian University of Thessaloniki, Thessaloniki, Greece. pp. 1449–  
 1605 1452, 2004.

1606 [Smith, A.J.B., Beukes, N.J., and Gutzmer, J.: The Composition and depositional environments of](#)  
 1607 [Mesoarchean Iron Formations of the West Rand Group of the Witwatersrand Supergroup, South](#)  
 1608 [Africa. Econ. Geol. 108, 111-134, 2013.](#)

1609 Sperling, E.A., Wolock, C.J., Gill, B.C., Kunzmann, M., Halverson, G.P., Macdonald,  
 1610 F.A., Knoll, A.H., and Johnston D.T.: Statistical Analysis of Iron Geochemical  
 1611 Data Suggests Limited Late Proterozoic Oxygenation. Nature 523, 451–454, 2015.

1612 Stewart, A. L. and Mcphie, J.: Facies architecture and Late Pliocene – Pleistocene  
 1613 evolution of a felsic volcanic island, Milo, Greece. Bull. Volcanol. 68, 703–726,  
 1614 2006.

Ernest C 23/2/2018 15:28

**Deleted:** Simonson, B. M.: Origin and evolution of large Precambrian iron formations. Geol. Soc. Am., 370, 231–244, 2003. ... (4)

Ernest Chi Fru 26/2/2018 10:50

**Formatted:** EndNote Bibliography, Indent: Left: 0 cm, Hanging: 0,5 cm, Don't add space between paragraphs of the same style, Line spacing: double

1620 Sun, S., Konhauser, K. O., Kappler, A., and Li, Y.-L.: Primary hematite in  
 1621 Neoproterozoic to Paleoproterozoic oceans. *GSA Bull.*, 127, 850–861, 2015.

1622 Stüben, D. and Glasby, G.P.: Geochemistry of shallow submarine hydrothermal fluids  
 1623 from Paleohori Bay, Milos, Aegean Sea. *Exp. Min. Geol.*, 8, 273–287, 1999.

1624 Swamy, V., Saxena, S. K., Sundman, B., and Zhang, J.: A thermodynamic assessment  
 1625 of silica phase diagram. *J. Geophys. Res. Solid Earth*, 99, 11787–11794, 1994.

1626 Taylor, J., and Parkes, R. J.: The cellular fatty-acids of the sulfate-reducing bacteria,  
 1627 *Desulfobacter* sp., *Desulfobulbus* sp. and *Desulfovibrio desulfuricans*. *J. Gen.*  
 1628 *Microbiol.*, 129, 3303–3309, 1983.

1629 Tice, M. M. and Lowe, D. R.: The origin of carbonaceous matter in pre-3.0 Ga  
 1630 greenstone terrains: A review and new evidence from the 3.42 Ga Buck Reef  
 1631 Chert. *Earth Sci. Rev.*, 76, 259–300, 2006.

1632 Tiodjio, R. M., Sakatoku, A., Nakamura, A., Tanaka, A., Fantong, W. Y., Tchakam,  
 1633 K. B., Tanyileke, G., Ohba, T., Hell, V. J., Kusakabe, M., Nakamura, S., and Ueda,  
 1634 A.: Bacterial and archaeal communities in Lake Nyos (Cameroon, Central Africa).  
 1635 *Sci. Rep.*, 4, 6151, DOI: 10.1038/srep06151, 2014.

1636 Trendall, A.F.: The significance of iron-formation in the Precambrian stratigraphic  
 1637 record. *Int. Assoc. Sed. Spe. Pub.*, 33, 33–66, 2002.

1638 Tsikos, H., Mathews, A., Erel, Y., and Moore, J.M.: Iron isotopes constrain  
 1639 biogeochemical redox cycling of iron and manganese in a Palaeoproterozoic  
 1640 stratified basin. *Earth Planet. Sci. Lett.*, 298, 125–134, 2010.

1641 van Hinsbergen, D. J. J., Snel, E., Garstman, S. A., Mărunțeanu, M., Langereis, C. G.,  
 1642 Wortel, M. J. R., and Meulen Kamp, J. E.: Vertical motions in the Aegean volcanic  
 1643 arc: evidence for rapid subsidence preceding volcanic activity on Milos and  
 1644 Aegina. *Mar. Geol.*, 209, 329–345, 2004.

Ernest Chi Fru 23/2/2018 20:46

**Deleted:** Stiegler, M. T., Lowe, D. R., and Byerly, G. R.: Abundant pyroclastic komatiitic volcanism in the 3.5-3.2 Ga Barberton greenstone belt, South Africa. *Geology*, 36, 779–782, 2008. .

Ernest C 23/2/2018 13:20

**Deleted:** Trower, E. J. and Lowe, D. R.: Sedimentology of the ~3.3 Ga upper Mendon Formation, Barberton Greenstone Belt, South Africa. *Pre. Res.*, 281, 473–494, 2016. .

1654 Varnavas, S. P. and Cronan, D. S.: Submarine hydrothermal activity off Santorini and  
1655 Milos in the Central Hellenic Volcanic Arc: A synthesis. *Chem. Geol.*, 224, 40–54,  
1656 2005.

1657 Weber, K. A., Achenbach, L. A., and Coates, J. D.: Microorganisms pumping iron:  
1658 anaerobic microbial iron oxidation and reduction. *Nat. Rev. Microbiol.*, 4, 752–64,  
1659 2006.

1660

1661

1662

1663

1664

1665

1666

1667

1668 Table 1. Table 1. Results of X-Ray Radiation (XRD) analysis showing major  
1669 mineralogical compositions. NFIF (non-fossiliferous iron formation) and MFIF  
1670 (microfossiliferous iron formation), respectively.

Mineral phase	MFIF1	MFIF2	MFIF3	Fe-rich NFIF2A	Si-rich NFIF2B	Fe-rich NFIF2C	Si-rich NFIFD	Fe-rich NFIF2E	Fe-rich NFIF2F
Hematite	+	+	-	+	+	+	+	+	+
Quartz	+	+	+	-	-	-	-	-	-
Sanidine	-	-	-	+	+	+	+	+	+
Tridymite	-	-	-	-	+	+	+	+	+
Cristobalite	-	-	-	+	-	-	-	-	-
Cryptomelane	-	-	+	-	-	-	-	-	-

1672

1673

1674

1675

1676

1677

1678  
1679  
1680  
1681  
1682  
1683  
1684  
1685  
1686  
1687  
1688  
1689  
1690  
1691  
1692  
1693  
1694  
1695  
1696  
1697  
1698  
1699  
1700  
1701  
1702  
1703  
1704  
1705  
1706

Table 2. Stable isotope results. Letters A-F on the NFIF samples represent respective bands of the sawn rock in Figure 7E.

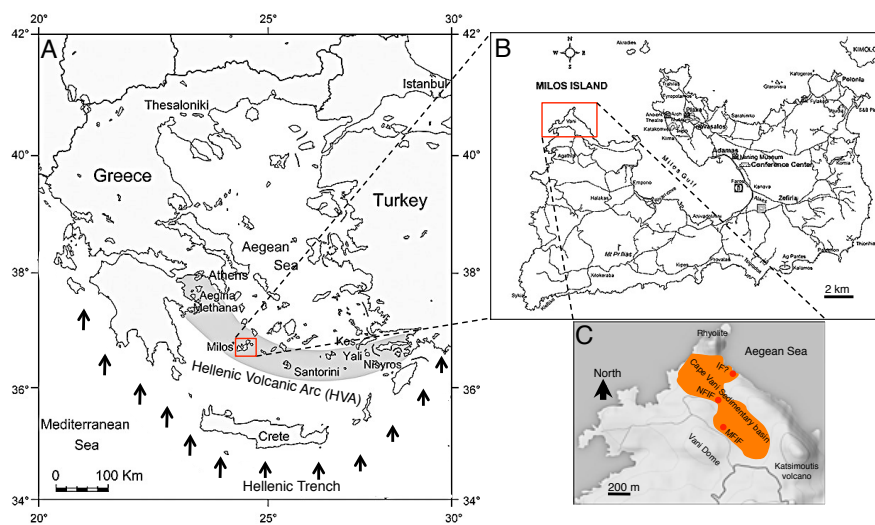
Sample	$\delta^{13}\text{C}_{\text{org}}$ vs PDB (‰)	$\text{C}_{\text{org}}$ (%)	$\delta^{15}\text{N}$ vs air (‰)	N (%)	$\delta^{34}\text{S}$ vs CDT (‰)	S (%)
Fe-rich NFIF2A	-25,63	0,061	nd	0,023	nd	0,01
Si-rich NFIF2B	-25,03	0,109	nd	0,017	nd	0,02
Fe-rich NFIF2C	-24,45	0,068	nd	0,013	nd	0,02
Si-rich NFIF2D	-25,04	0,076	nd	0,015	nd	0,02
Fe-rich NFIF2E	-25,19	0,042	nd	0,009	nd	0,01
Si-rich NFIF2F	-25,49	0,050	nd	0,012	nd	0,03
MFIF1	-25,49	0,087	nd	0,017	nd	0,01
MFIF2	-26,25	0,046	nd	0,005	nd	nd
MFIF3	-25,69	0,041	nd	0,006	nd	nd

ND, Not detected

1709  
1710



1711  
1712  
1713  
1714  
1715  
1716  
  
1717  
  
1718  
  
1719  
  
1720  
  
1721  
  
1722  
  
1723  
  
1724  
  
1725  
  
1726  
  
1727



1728

1729 Fig. 1. Geological map of Milos (redrawn from Marschik et al., 2010). (A),  
1730 Geotectonic map showing the position of Milos Island, along the Hellenic Volcanic

Arc (HVA). Arrows indicate the direction of subduction of the African plate underneath the Euroasian plate. (B) Milos Island. (C), The Milos iron formation is located in the 8-shaped Cape Vani sedimentary basin (CVSB). At least two IFs are present in the CVSB. These are made up of a non-fossiliferous IF (NFIF) at the juncture between the two large sedimentary basins and a microfossiliferous iron formation (MFIF) located at the SW margin in the second basin. A potential third IF (IF?) is located NE, close to the present day Aegean Sea. It is however not certain if this deposit is part of the NFIF or not, because of the open mining pit separating the two.

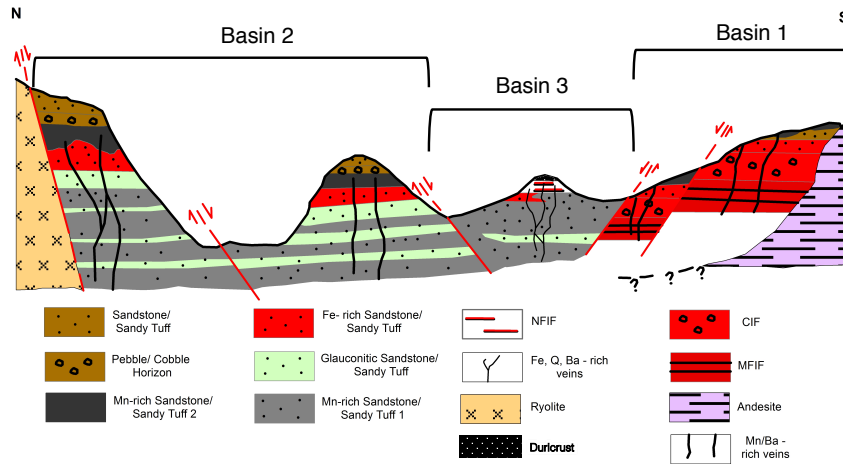


Fig. 2. Generalized schematic north-south geologic cross section through the ~1 km long CVSB showing interpreted geology, relationships between the main lithofacies, main fault locations, the iron and manganese formations, in support of a proposed three-basin hypothesis. Not drawn to scale. Four types of iron-rich sedimentary rocks occur in the CVSB. These include the iron-rich sandstones, the iron-Mn-rich sandstones, the conglomerate hosted iron formation (CIF) and the MFIF and NFIF formations that are depositionally and chemically distinct from the sandstone deposits.

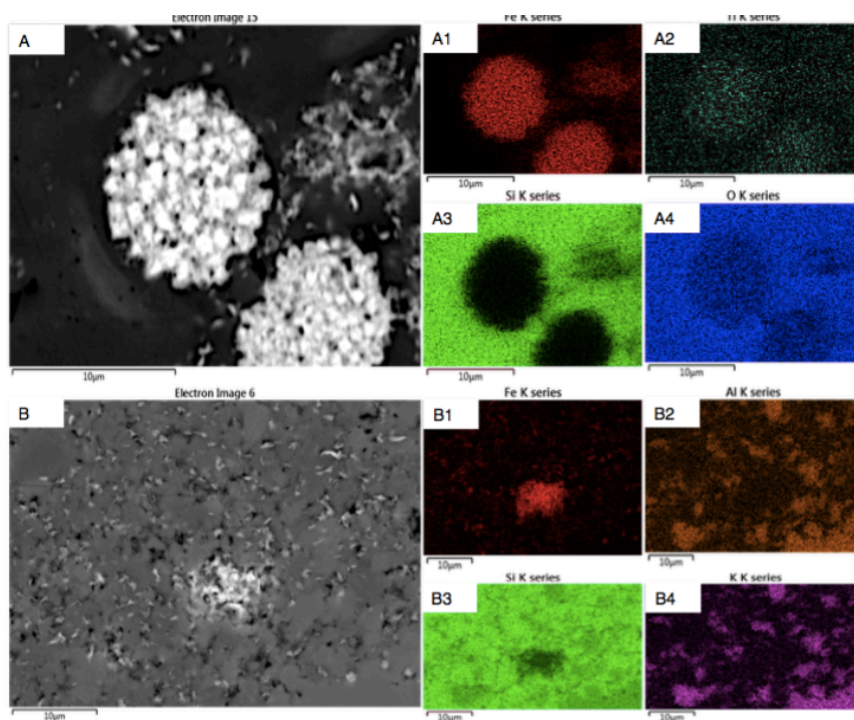


Fig. 3. EDS-electron image showing different Fe-rich mineral phases in a Si-rich matrix from the MFIF. The bright colours correspond to the analysed elements. (A), framboidal hematite particles. A1-A4, different element compositions associated with framboidal particles in panel A. (B), Dispersed fluffy Fe-rich mineral grains. B1-B4, corresponding elements associated with the micrograph in panel A.

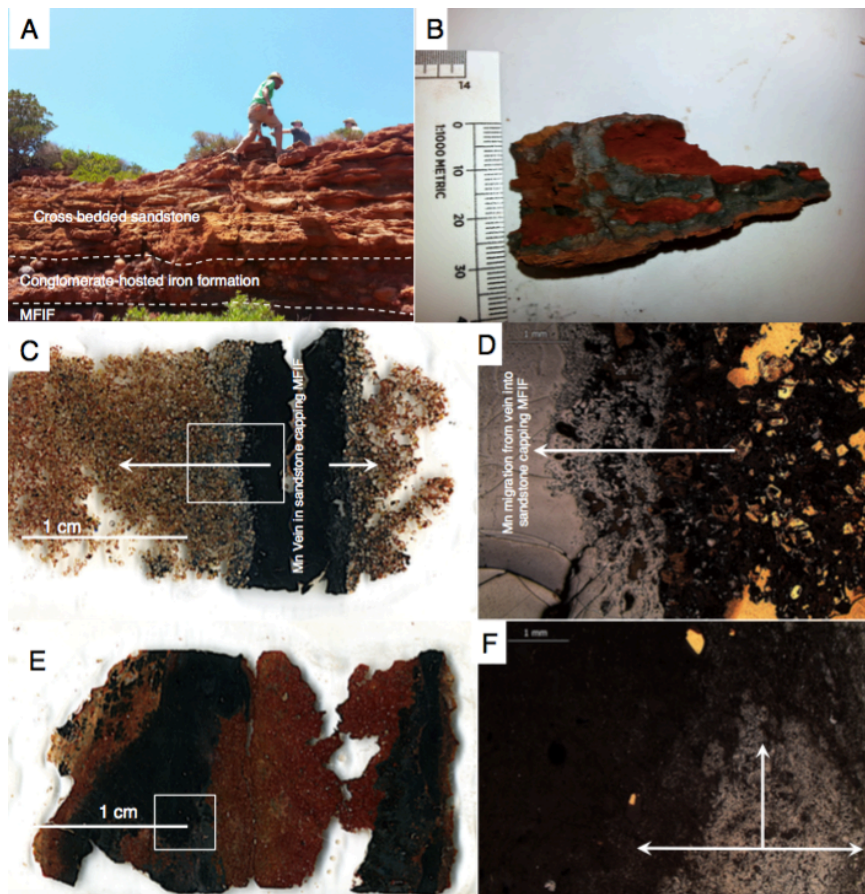
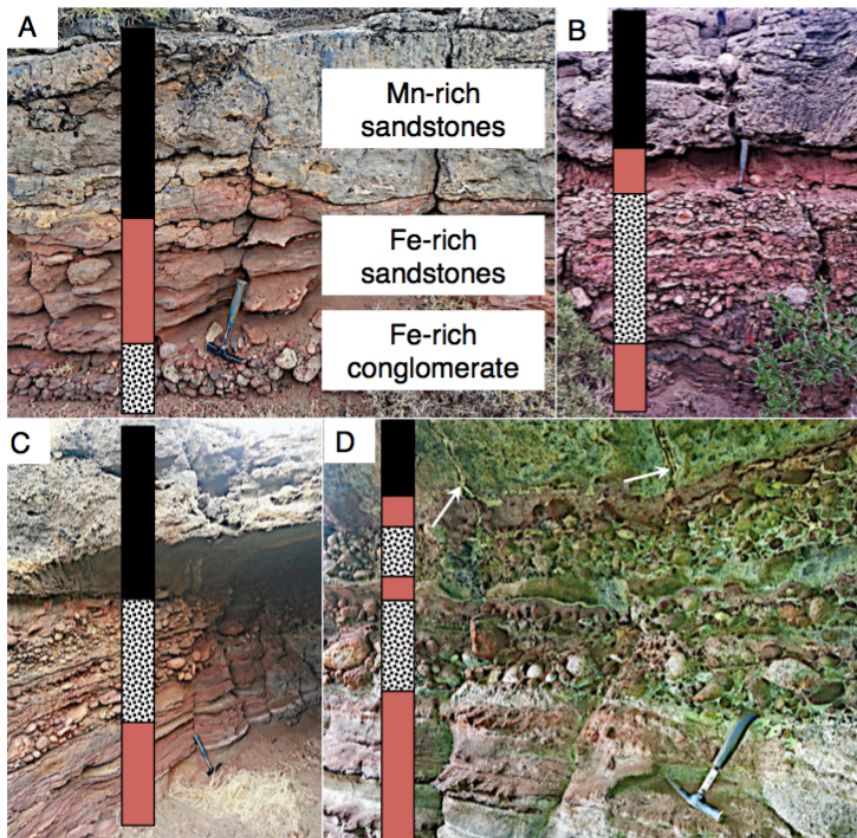


Fig. 4. Sedimentary profile, thin section scans and optical microscope images of the MFIF. (A), Field photo showing the sedimentary profile of the MFIF characterized by the overlying sandstone cap. (B), Photograph showing black diffused Mn-rich bands near the base of the MFIF. (C), Scanned image of thin section showing a black Mn-rich vein in the overlying MFIF sandstone showing a gradient of Mn migrating into the sandstone matrix (white arrows). (D), Light microscopy images showing details in panel C. (E), Scanned image of an MFIF thin section showing black Mn bands migration into a red iron-rich background. (F), Amplified light microscope image showing gray Mn layers migrating into a black Fe-rich matrix. White arrows show direction of movement. Boxes in C and E are amplified in D and F.





1774

1775 Fig. 5. Sedimentary sequence overlying the MFIF, consisting of thin (< 0.5 m)  
 1776 polymictic andesite-dacite cobble-pebble, and sandstone-sandy tuff pebble, and Fe-  
 1777 rich conglomerate facies overlain by thinly laminated Fe-rich sandstone beds. This  
 1778 vertical sequence is interpreted to represent a progressively deeper water environment  
 1779 deepening-upward sequence (A) as a result of sea level rise due to tectonic  
 1780 subsidence. The multiple cycles shown in panels B-D signify several potential  
 1781 episodes or sea level rise. Arrows in panel D showing hydrothermal feeder veins  
 1782 feeding the overlying layers. The sequence is overlain by a thin package of parallel  
 1783 and cross-bedded Mn-sandstone cap.  
 1784

1785

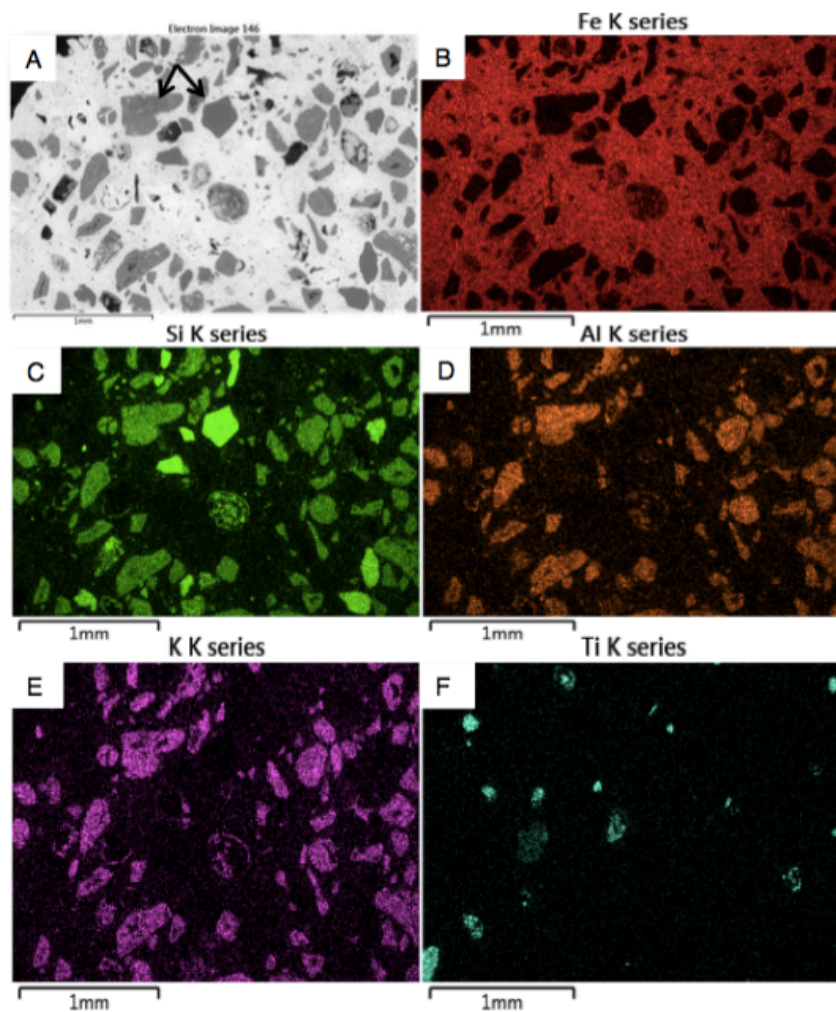


Fig. 6. Scanning electron microscope electron image of the volcaniclastic (K-feldspar)/ iron-rich sandstone conglomerate overlying the MFIF.

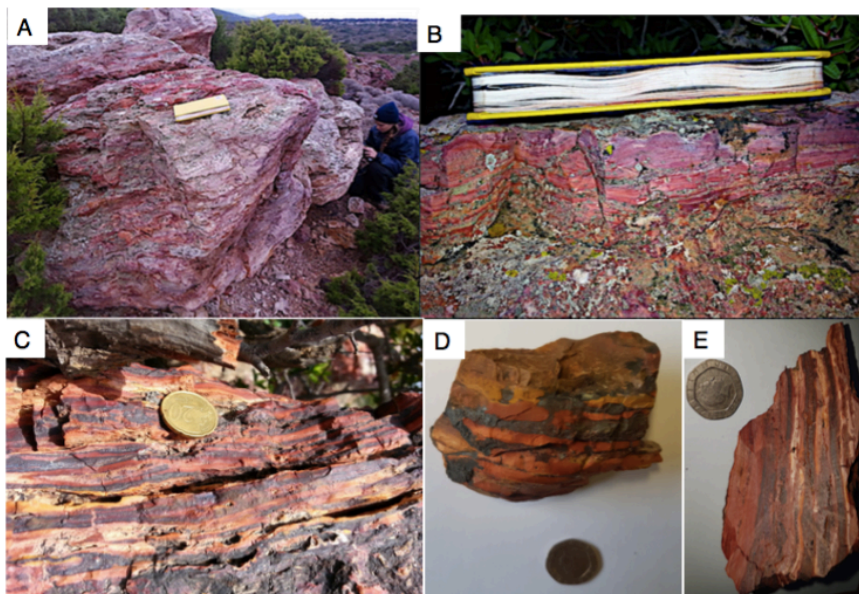


Fig. 7. Typical NFIF banded iron rocks. (A-C), Field photographs. (D), Handheld banded Fe sample. (E), Sawn NFIF sample with laminated Fe-rich bands alternating with Si-rich bands.



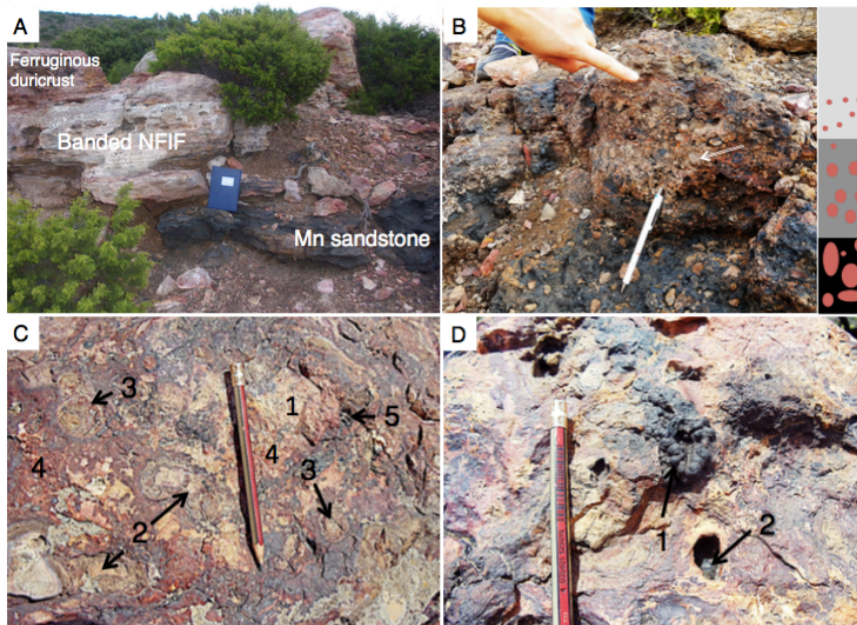
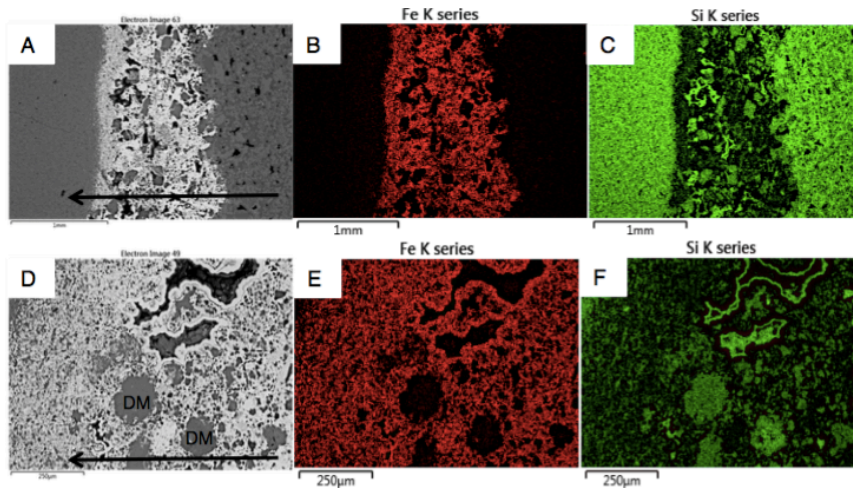


Fig. 8. Field sedimentology and stratigraphy of Section B sequence containing the NFIF. (A), Sharp boundary between lower Mn sandstone and unconformably overlying NFIF capped by a ferruginous duricrust. (B), Sandstone-sandy tuff pebble to gravel conglomerate lag facies, showing an upward fining character and bored clasts (black), locally overlies the Mn sandstone and capped by a sharp erosional contact with the overlying NFIF. The tip of the pen (7 cm long) rests on late blue-black Mn oxide overprint. (C), Ferruginous duricrust that comprises lithic fragments composed of (1) Fe-nodules (2) and Fe-concretions (3) in a hematite-rich matrix (4). (D), Matrix dissolution resulting in vermiform Mn nodules (1) and cavity black Mn oxide (2) infillings, post-dating the ferruginous duricrust formation.





1810

1811 Fig. 9. EDS-electron image showing major elemental composition of typical Fe bands  
 1812 alternating with Si-rich layers in the NFIF. Volcaniclastic detritus mostly present in  
 1813 the Fe-rich bands, suggests precipitation during active submarine volcanism. To the  
 1814 contrary, the Si-rich bands are composed of more fine-grain, signifying deposition  
 1815 during periods of minimal volcanic activity. Arrows in panels (A) and (B) depict the  
 1816 direction of sedimentation, which was often seen to proceed from an Fe-rich matrix  
 1817 mixed with large grains of volcaniclastic detritus (DM) to one composed essentially  
 1818 of very fine-grained Fe particles before transitioning into the very fine-grained Si-rich  
 1819 layer. An upward fining of the volcaniclastic particles in the Fe-rich layers transitions  
 1820 from one made up of volcaniclastic debris and hematite, to a mainly thin hematite-  
 1821 rich horizon at the top of this mixed layer (see supplementary Figs 8-11 for details).  
 1822 This concurrent occurrence of volcaniclast and Fe oxides and the upward fining  
 1823 nature of the Fe-rich layers, suggest the release and oxidation of Fe(II) coincided with  
 1824 the settling of hydrothermal debris resulting from the introduction of enormous  
 1825 amount of reduced materials into the water column (Bekker et al., 2010). The iron-  
 1826 rich layer ceased forming as hydrothermal/volcanic release of Fe subsided, followed  
 1827 by deposition of the Si-rich layer. This repetitive cycle of events is observed for tens  
 1828 of metres laterally and vertically, stressing that the layers are not single isolated or  
 1829 post-depositional replacement events, but chemical precipitates that sequentially  
 1830 sedimented out of the water column. Red colour in Panels (B) and (C) depict Fe and  
 1831 green in panels (C) and (F), Si.

1833

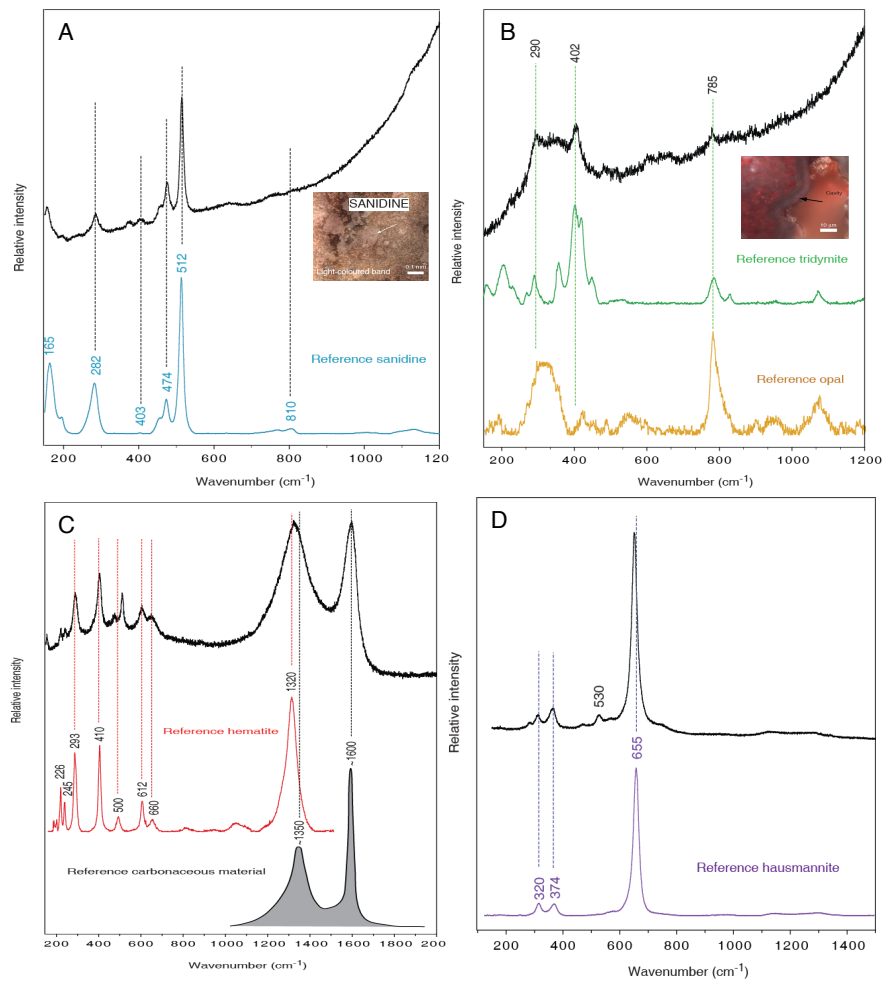
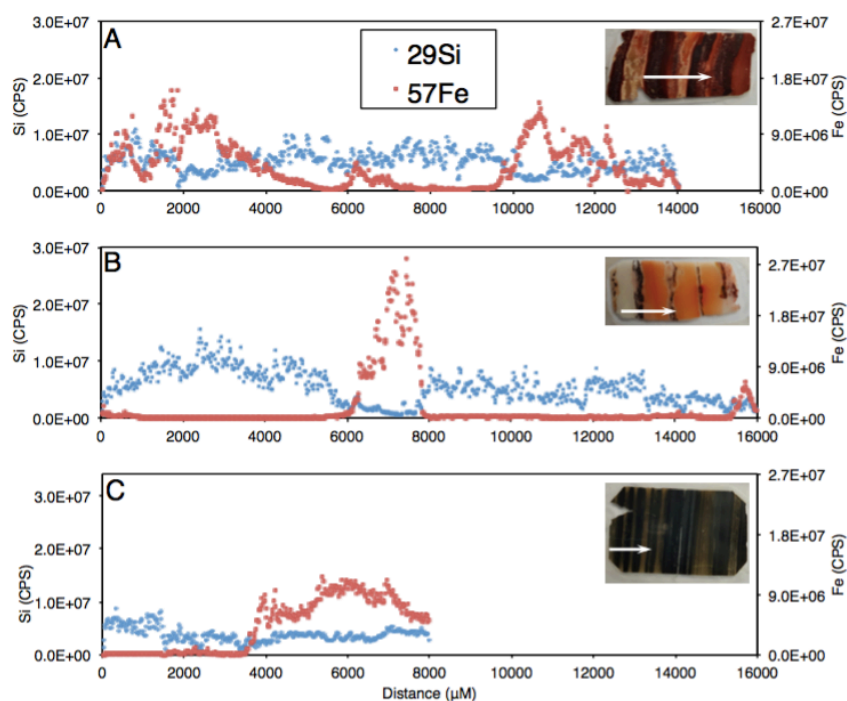


Fig. 10. Raman spectroscopy of the Fe- and/or Si-rich bands from NFIF.



1837

1838 Fig. 11. Fluctuation in Si and Fe content measured by in situ laser ablation ICP-MS  
 1839 analysis. (A), Milos BIF-type rock with evenly distributed Si and iron rich bands. (B),  
 1840 Milos BIF type rock with large Si bands (whitish-brownish strips) and narrow Fe-rich  
 1841 bands (dark strips). (C), An example for the 2.5 Ga Kuruman BIF. Insets are analyzed  
 1842 thin sections. For scale, each thin section is  $\approx 3.3$  cm long. White arrow on thin section  
 1843 indicates analyzed area.

1844

1845

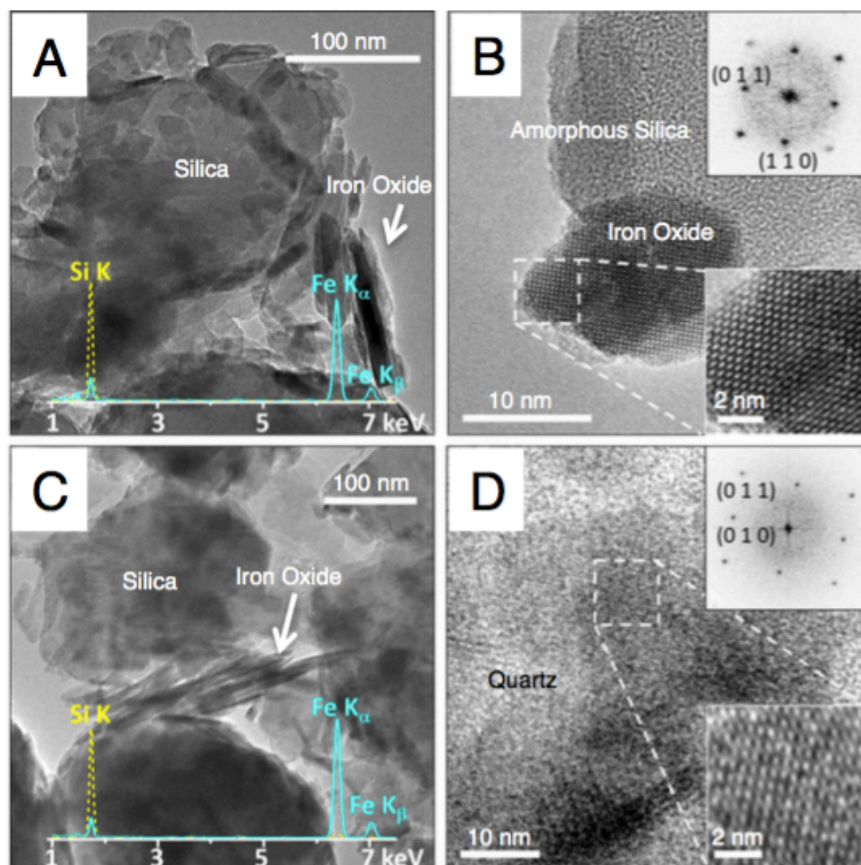


Fig. 12. TEM characterization of an NFIF and MFIF specimen. (A) lower magnification MFIF TEM-BF image. (B) High resolution images of NFIF showing amorphous Si and iron oxide crystalline lattice structures. Insets highlight a hematite particle viewed from the [1-11] axis (Rhombohedral lattice). (C) Lower magnification MFIF TEM-BF image. (D) High resolution images of MFIF showing crystalline quartz and iron oxide crystalline lattice structures. Insets in (D) show a quartz crystal viewed from the [100] axis. Both samples contain silica with a few hundred nm particle size, and smaller needle-like iron oxide particles. Spectral lines in panels (A) and (C) are X-ray Energy Dispersive elemental profiles of the individual Fe and Si mineral phases.

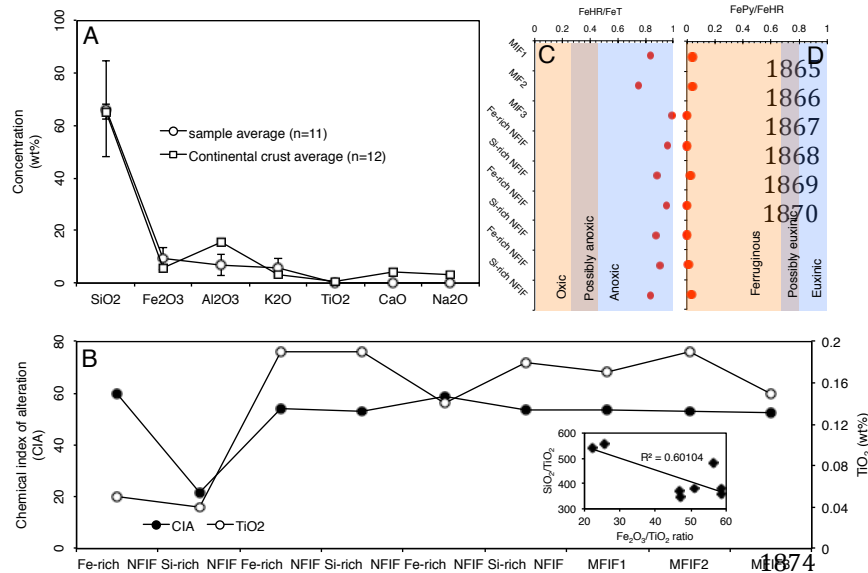


Fig. 13. Bulk average concentrations of major trace elements, chemical weathering indices and reconstructed redox depositional conditions for typical MFIF and the Fe/Si-rich NFIF and for the sawn rock sample in Figure 7E. (A), Relationship between average major trace element content and average continental crust (Rudnick and Gao, 2003). (B), Chemical Index of Alteration (CIA). Inset, relationship between SiO<sub>2</sub> and Fe<sub>2</sub>O<sub>3</sub>. (C) Highly reactive Fe (FeHR) to Total Fe ratio (FeT). (D) Pyrite to FeHR ratio.

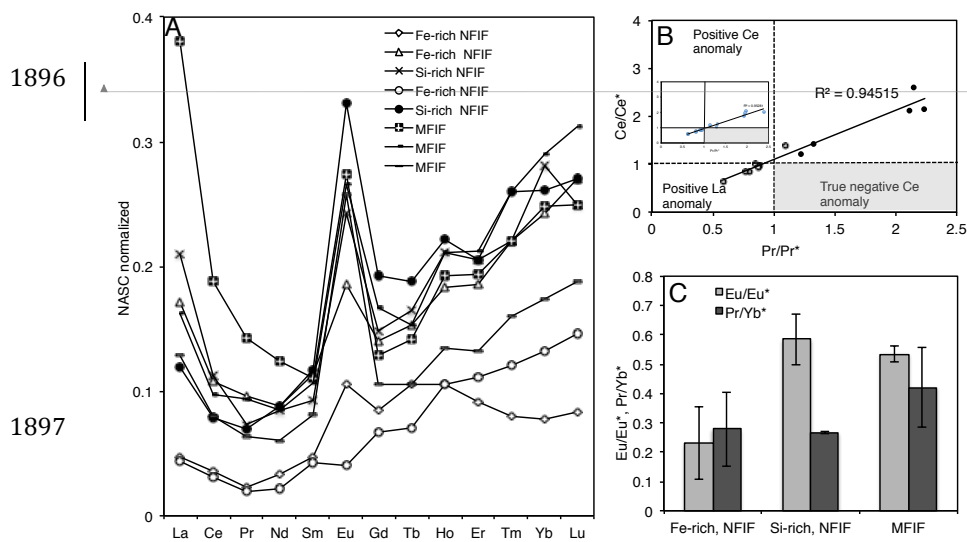
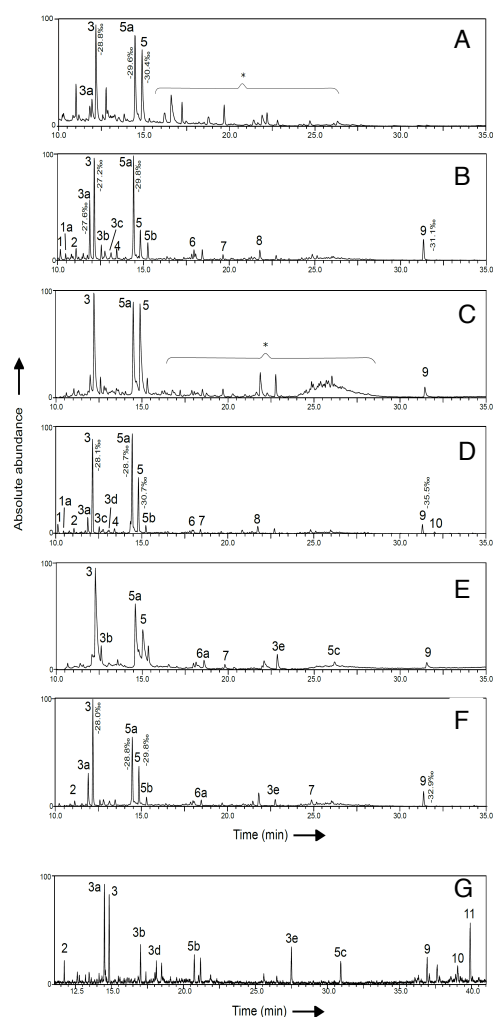


Fig. 14. Rare earth element (REE) distribution in samples and calculated Ce and Eu anomalies. (A), NASC normalized REE distribution in various rock facies. (B), Ce and Eu anomalies. (C), Eu anomalies and light REE (LREE) vs. heavy REE (HREE). Similar trends were reproduced when REE data were normalized with the Post Archean Australian Shale standard (McLennan, 1989; Bau and Dulski, 1986). This is exemplified by the insert in B.



1904

1905 Fig. 15. GC/MS chromatogram sections of total lipid extracts of the BIF (A-F) for  
 1906 bands excised from the sawn rock in Figure 7E. Panel G illustrates a total lipid extract  
 1907 of modern sediment from the Milos basin. Values beside peaks indicate the lipid-  
 1908 specific  $\delta^{13}\text{C}$  values in per mil. Because of the low intensity of the lipids recovered, it  
 1909 was not possible to obtain  $\delta^{13}\text{C}$  values specific for all peaks. Peaks are annotated as;  
 1910 FAME = fatty acid methyl ester; Me = methyl group; TMS = trimethylsilyl; TMSE =  
 1911 trimethylsilyl ester. (1)  $\text{C}_{14:0}$  FAME, (1a)  $\text{C}_{14:0}$  13Me FAME, (2)  $\text{C}_{15:0}$  FAME, (3)  
 1912  $\text{C}_{16:0}$  FAME, (3a)  $\text{C}_{16:9}$  FAME, (3b)  $\text{C}_{16:0}$  TMS, (3c) 10Me  $\text{C}_{16:0}$  FAME, (3d)  $\text{C}_{16:9}$   
 1913 FAME, (3e)  $\text{C}_{16:0}$  TMSE, (4)  $\text{C}_{17:0}$  TMS, (5)  $\text{C}_{18:0}$  FAME, (5a)  $\text{C}_{18:9}$  FAME, (5b)  $\text{C}_{18:0}$   
 1914 TMS, (5c)  $\text{C}_{18:0}$  TMSE, (6)  $\text{C}_{19:0}$  FAME, (6a)  $\text{C}_{19:0}$  18Me TMS, (7)  $\text{C}_{21:0}$  TMS, (8)

1915 C<sub>22:0</sub> TMS, (9) Cholesterol TMS, (10) Stigmasterol TMS, (11) beta-Sitosterol (\*)  
1916 contaminants (e.g., phthalates).  
1917

1918

1919

1920

1921

1922

1923

1924

1925

1926

1927

1928

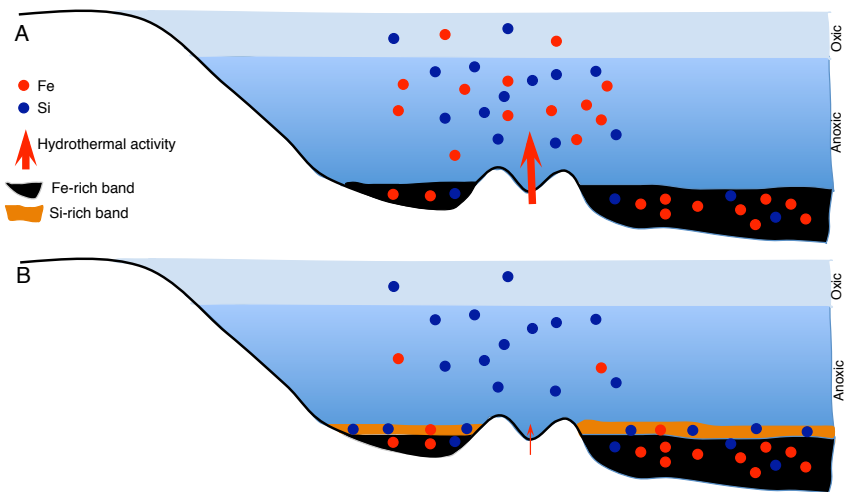
1929

1930

1931

1932





1933

1934 Fig. 16. Conceptual model showing the mechanism of band formation in the NFIF  
 1935 related to changes in the intensity of hydrothermal activity and chemical oxidation of  
 1936 Fe(II) to Fe(III) in the water column, inferred directly from our data. See Chi Fru et  
 1937 al. (2013) for a biological model for the formation of the MFIF.